Summer 2003

A Forward-Backward Fluence Model for the Low-Energy Neutron Boltzmann Equation

Gary Alan Feldman
Old Dominion University

A FORWARD-BACKWARD FLUENCE MODEL FOR THE LOW-ENERGY NEUTRON BOLTZMANN EQUATION

by

Gary Alan Feldman
A.A. June 1980, Oakland Community College
B.S. May 1987, Texas A & I University
M.S. August 1990, Southwest Texas State University

A Dissertation Submitted to the Faculty of
Old Dominion University in Partial Fulfillment of the
Requirement for the Degree of

DOCTOR OF PHILOSOPHY

COMPUTATIONAL AND APPLIED MATHEMATICS

OLD DOMINION UNIVERSITY
August 2003

Approved by:

John Tweed (Director)

John H. Heinbockel (Member)

Martha S. Clowdsley (Member)

Fang Q. Hu (Member)

ABSTRACT

A FORWARD-BACKWARD FLUENCE MODEL FOR THE LOW-ENERGY NEUTRON BOLTZMANN EQUATION

Gary Alan Feldman
Old Dominion University, 2003
Director: Dr. John Tweed

In this research work, the neutron Boltzmann equation was separated into two coupled integro-differential equations describing forward and backward neutron fluence in selected materials. Linear B-splines were used to change the integro-differential equations into a coupled system of ordinary differential equations (O.D.E.'s). Difference approximations were then used to recast the O.D.E.'s into a coupled system of linear equations that were solved for forward and backward neutron fluences. Adding forward and backward fluences gave the total fluence at selected energies and depths in the material. Neutron fluences were computed in single material shields and in a shield followed by a target configuration. Comparison was made to Monte Carlo modeling of the Boltzmann equation for the same material configuration. Slabs of aluminum, copper, and Martian regolith served as single material shields. The Forward-backward model fluences are accurate for energies above 4 MeV at all depths in these media. There is less accuracy for energies below 4 MeV, but the forward-backward model results are more accurate than past calculations and provide approximately an order of magnitude improvement. An aluminum shield followed by a water target configuration was also investigated using the forward-backward model. The resulting fluence is accurate in the aluminum shield, but less accurate in the water target. It is suspected that this is largely due to inaccuracies in the material cross sections that were used in the modeling.

This dissertation is dedicated to my parents,
Dr. Herbert O. Feldman and Mrs. Charlotte F. Feldman.

ACKNOWLEDGMENTS

I want to express my deep gratitude to all the members of my dissertation committee. Their comments and suggestions were extremely helpful in editing this manuscript. I have learned much from Dr. John H. Heinbockel during my education at Old Dominion University. He helped me whenever I encountered difficulties with this research work. Many times Dr. Martha S. Clowdsley answered my questions regarding radiation protection research and computer related matters. Dr. John Tweed and Dr. Fang Q. Hu helped me whenever I requested their assistance. I also want to thank Dr. Robert C. Singleterry for sharing with me his knowledge of low-energy neutron transport modeling. Finally, I want to thank Dr. John W. Wilson of NASA Langley Research Center for supporting this work under NASA research grant NCC-1-404.

TABLE OF CONTENTS

LIST OF TABLES

LIST OF FIGURES

CHAPTER I

INTRODUCTION

Neutrons are produced when shielding materials are bombarded by solar and galactic particles during space travel and high altitude flight. Researchers want to protect human life and electronic equipment from the products of neutron interaction with materials. The Boltzmann equation for the transport of low-energy neutrons was solved using the forward-backward fluence model described in this paper. The solutions were added to the NASA Langley Research Center High Charge and Energy Transport (HZETRN) code results for higher energy neutrons. This produced accurate results and required shorter solution times than Monte Carlo methods. The information given in the following two sections discusses the history of space radiation research, and was drawn from reference [1].

Space Radiation Research Prior to NASA

In 1949, C.F. Gell suggested at the panel meeting on the Aero Medical Problems of Space Travel, that space radiation may be life threatening. He thought there was a possibility that cosmic radiation was unable to penetrate the Earth's atmosphere and may have an effect on the health of pilots. He also surmised that many particles are deflected away from the Earth by its geomagnetic field, causing them to be unobserved during stratospheric flight experiments. The presence of radiation fields led to an investigation of the need for protection from space radiation.

The model journal used is *Nuclear Science and Engineering*.

In 1950, H.J. Schaefer of the Naval School of Aviation determined that the number of cosmic rays is relatively small near the Earth's surface. Schaefer went on to state that the number of cosmic rays increases steadily with increasing altitude up to 70,000 feet. Above 70,000 feet he suggested the number decreases for some distance, and then increases again. Schaefer attributed the increase to ionization produced by "heavy nuclei rays" with low penetrating power.

Krebs in 1950, at the Field Research Laboratory of the Army Medical Service, suggested that cosmic air showers are due to "explosive nuclear stars created by heavy nuclei coming from outside the atmosphere," and could have biological effects. This was a departure from Schaefer's notion of direct ionization of cosmic heavy nuclei. Two years later in 1952, Schaefer was the first to argue that linear energy transfer (LET) from radiation to a biological system may not be a good way to predict how the system will respond because the track width the radiation creates also controls the biochemistry. LET measures the energy deposited per unit distance over the path of the radiation[2]. Both Krebs and Schaefer made fundamental contributions to the fields of radiation physics and biology that are still important today.

Presented at the Symposium on Space Medicine in 1952 was a paper by C.A. Tobias on the radiation hazards of flying at high altitudes. He stated that it would be advantageous to look for low-energy cosmic nuclei near the North Pole since the Earth's magnetic effects are minimal there. He also proposed that the fragmentation of heavy ions would produce less ionizing secondaries, which may turn out to be less hazardous. At that time, no ground-based facility could accelerate iron nuclei to high enough energies to measure the Relative Biological Effectiveness (RBE), and flight experiments

are not very fruitful due to the limited amount of exposure time to cosmic ray nuclei. This made it difficult to experimentally measure the effects of radiation on biological systems. Then on February 23, 1956 there was a spectacular solar flare that allowed for a resurgence of investigation into space radiation. In 1958, NASA was formed and Van Allen discovered the Earth's radiation belts. This precipitated the possibility of space travel, which had to take into account effects of the Van Allen radiation belts.

Space Radiation Research at NASA

There was a very important NASA conference in June 1960 where several factors relevant to solar flare events were discussed. These factors included how different locations on the Sun affect the Earth, the propagation of radiation from the Sun to the Earth, geomagnetic effects, estimation of shielding thickness, and other topics. Winckler suggested that being exposed to Galactic Cosmic Radiation (GCR) during missions that last for short periods of time would probably not have any harmful effects. It was suggested by J.E. Pickering that radiation risk should be consistent with other risks encountered during a mission, and this became the operational rule regarding risk due to radiation.

Space radiation protection research began at NASA Langley Research Center in 1958. Researchers were mainly concerned with contributions from scattering events involving neutrons and targets that recoil during collisions. In 1962, there was the first Symposium on the Protection Against Radiation Hazards in Space in Gatlinburg, Tennessee, where it was announced the Space Radiation Effects Laboratory at Langley would be constructed. Today, this is the location of the Jefferson Laboratory, formerly

known as the Continuous Electron Beam Acceleration Facility (CEBAF). Experiments were conducted at this laboratory to bring about increased protection from secondary particles produced during the collisions of protons and alpha particles. The High-Energy Transport Code (HETC) was also introduced at the conference. This code has been developed and continues to be improved upon.

In 1965, an atmospheric measurements program was initiated, but due to a lack of funds the program was discontinued in January 1972. Two important papers were presented at the second Gatlinburg conference in 1965. One paper was by P. Todd, which discussed the effects of high-energy heavy ions on cell survival. The other paper was written by S.B. Curtis and was also in reference to high-energy heavy ions. The High-Energy Transport Code was reported in several papers at the conference to be an important research tool. One paper by R.G. Alsmiller, Jr. demonstrated how the straight-ahead approximation for high-energy nucleon transport could be applied to space radiations. The research at NASA Langley Research Center in particle transport theory has been greatly influenced by this seminal paper.

In 1965, in conjunction with the Korff group at New York University, NASA Langley implemented a program to measure solar flare events using flight experiments. These experiments utilized both airplanes and balloons to acquire the measurement data. A year after this program began at NASA Langley; the International Commission for Radiological Protection (ICRP) Task Group for Supersonic Transport (SST) exposure published a paper stating the effects on biological systems exposed to atmospheric neutrons were negligible. Researchers at NASA Langley then attempted to include in the measured neutron spectrum lower and higher energies by using the High-Energy

Transport Code developed at Oak Ridge National Laboratory. This code utilized the Monte Carlo method to compute particle fluence. Bertini, in 1967, developed a nuclear reaction code that included the internuclear cascade calculation. This code made the reliance on external nuclear databases less important, however, the time needed to perform the internuclear cascade calculation greatly extended the run time of the entire code to where it became impractical and inefficient. In order to get access to the High-Energy Transport Code, researchers at NASA Langley Research Center had to wait in line with accelerator, biomedical, dosimetry, and space programs researchers. This was an unacceptable situation, so researchers at NASA Langley decided to develop their own codes.

The code PROPER-C was written by Leimdorfer and Crawford in 1968 at NASA Langley for low-energy applications. This code was later extended to include high energies and took on the name PROPER-3C. The code developed at Langley was fast but required over $80,000 of computer time to extend the neutron spectrum to high energies. Even with the results generated from the code, the amount of background radiation was still uncertain because transition curves of other heavy primary ions were not known, and heavy ions may make contributions to the dose equivalent for some solar flare events. The dose equivalent is obtained by multiplying absorbed dose by a quality factor of the radiation. The possible effects of radiation on humans lead researchers to study heavy ion reactions at the Princeton Particle Accelerator. These experiments were later moved to Lawrence Berkeley Laboratory, and have been carried out there up to this day.

Due to the shortage of nuclear data, the need for a theoretical nuclear program became crucial. The Monte Carlo method was yielding good results, but required a tremendous amount of computer resources to do so. In the early 1970's, this lead to the development of a multiple scattering theory, a fundamental theory of heavy ion reactions, and a database for heavy ion cross sections. NASA Langley was moving away from the Monte Carlo methods giving preference to deterministic codes in nucleon transport and heavy ion transport theory. At the third Gatlinburg conference, the biological effects of exposure to galactic cosmic rays on long duration missions were discussed.

Unfortunately, funding became sparse at NASA Langley from 1973 to 1980 and the amount of research performed during this time suffered as a result. A proposal submitted on July 31, 1979, by John Wilson to the Life Sciences Division of NASA Langley Research Center lead to the restoration of space radiation protection research at NASA Langley Research Center. The Baryon Transport (BRYNTRN) deterministic code was developed at NASA Langley Research Center in 1989 to model proton transport. The code was faster than previous codes and was later modified to include the transport of neutrons and alpha particles. The HZETRN deterministic code was developed in 1995 at NASA Langley Research Center to compute the transport of heavy ions in materials. The BRYNTRN code was later incorporated into the HZETRN code.

Applications of a Fast and Accurate Radiation Transport Code

A radiation transport code has applications in the engineering design of objects and materials that shield biological systems and electronic components from radiation. People are continuously being exposed to radiation that is emanating from various

sources in the universe. The radiation comes from materials that reside in the Earth, and from objects in outer space. When measuring radiation, a millirem (mrem) is the unit of measurement frequently used. A rem (*r*oentgen *e*quivalent *m*an) is the product obtained by multiplying the number of rads with a quality factor that converts rads from different types of radioactivity into a common scale of biological damage[2-3]. A rad of radiation equals 100 ergs per gram, and 1 sievert equals 100 rads. A person on average is exposed to a dose of about 360 mrems per year[4-8]. International Standards allow people that work around radioactive material to be exposed to as much as 5,000 mrems in a single year[4-8]. A jet pilot is exposed to about 0.5 mrem per hour that he or she is in the air[4-8]. Having adequate radiation shielding is therefore important to the safety of jet pilots who spend many hours in flight.

Without adequate radiation shielding, NASA's vision of one day sending a crew safely to Mars will not be realized. A radiation transport code is needed to determine the amount of radiation a crew will be exposed to on such a long journey. Another application of the HZETRN code is to determine the amount and types of radiation shielding needed on the International Space Station (ISS). To protect crewmembers, shielding materials must inhibit the passage of harmful space radiation without adding an undue amount of weight to the ISS. "Data collected by NASA and a Russian-Austrian collaboration shows that astronauts on the ISS are subjected to about 1 millisievert of radiation per day, about the same as someone would get from natural sources on Earth in a whole year. Spending three months in these conditions translates into about one-tenth the long-term cancer risk incurred by regular smokers[9-10]." The risk will increase even more by sending astronauts out beyond the Earth's magnetic field. According to Marco

Durante of the Federico II University in Naples, if two people are sent to Mars only one of them will survive[9].

Cosmic rays are composed largely of high-speed heavy ions. When cosmic rays collide with aluminum inside the ISS, a shower of secondary particles are produced that can be very harmful to the crew living on board. Polyethylene has lighter atomic nuclei than Aluminum, and will release fewer light ions and neutrons than Aluminum when bombarded by cosmic rays. For this reason, additional polyethylene shielding has been placed on the ISS. A lowering of only a few percent in the astronaut's exposure has been measured as a result of adding polyethylene shielding. To remove more of the exposure requires more shielding, which adds weight to the ISS. To overcome this problem, Frank Cucinotta, a space radiation protection research scientist at NASA Johnson Space Center in Houston, Texas, said "entirely new shielding technologies will have to be developed, and no one knows how long that might take[9]."

The US Environmental Protection Agency (EPA) has determined that no one should receive a dose of radiation that increases their relative risk of dying from cancer by over 3 percent, and NASA uses this value as the dose limit for allowable radiation exposure[9,11]. According to Cucinotta the radiation risk on the ISS is 5 percent[9]. Durante disagrees with this finding. He calculated a 20 percent higher risk of dying from cancer, which is not within the limits set by NASA[9]. The radiation levels beyond a low Earth orbit increase by a factor of three or four which makes it potentially very dangerous for astronauts to carry out their missions[9]. A good radiation transport code must calculate the fluences of all particles in the radiation field to give an accurate estimate of astronaut risk. Neutrons are an important component of the radiation field. Low-energy neutrons

scatter isotropically and are modeled separately from other neutrons. The forward-backward model is used to calculate the low-energy neutron fluence component of the radiation field.

Objective of this Dissertation

The HZETRN code has proven to be accurate in computing neutron fluence in various materials at energies above 30 MeV, but at lower energies inaccuracies are present. A low-energy neutron equation is developed to accurately model the isotropic scattering of neutrons at energies less than 30 MeV. A forward-backward approximation is applied to this model. Forward-backward model isotropic evaporation neutrons are added to HZETRN code forward moving high-energy neutrons to give the neutron fluence at all energies. The resulting neutron fluence is compared with Monte Carlo simulations of neutron fluence over all energies. The forward-backward model improves on HZETRN results for neutron energies less than 30 MeV in single material shields. This dissertation is a continuation of the space radiation protection research work done at NASA Langley Research Center.

CHAPTER II

NEUTRON PHYSICS

Following the analysis in reference [12], physical processes involving neutrons are investigated. Neutrons are produced in materials by neutron-induced fission, and by other processes as well. Table I shows a comparison of the rates at which different heavy nuclides will spontaneously fission to produce neutrons. In the table, $T_{1/2}$ (Fission) represents the half-life of the nuclide to decay by releasing neutrons through spontaneous fission, and $T_{1/2}$ (α - decay) represents the half-life of the nuclide to decay by releasing α - particles. Heavy nuclides that undergo spontaneous fission emit harmful radiation, and are not used for shielding purposes.

Table I
Neutron Production by Spontaneous Fission.

Nuclide	$T_{1/2}$ (Fission)	$T_{1/2}$ (α-decay)	neutrons/sec/gram
$^{235}_{92}U$	1.8×10^{17} years	6.8×10^{8} years	8.0×10^{-4}
$^{238}_{92}U$	8.0×10^{15} years	4.5×10^{9} years	1.6×10^{-2}
$^{239}_{94}Pu$	5.5×10^{5} years	2.4×10^{4} years	3.0×10^{-2}
$^{240}_{94}Pu$	1.2×10^{11} years	6.6×10^{3} years	1.0×10^{3}
$^{252}_{98}Cf$	66.0 years	2.65 years	2.3×10^{12}

Neutrons that are produced from sources other than neutron-induced fission are commonly referred to as source neutrons. Neutrons that are generated by the fission process on average have 2 MeV of energy. Liberated neutrons interact with their

environment through scattering and absorption processes. Scattered neutrons lose energy and after a sufficient number of interactions become thermalized. Thermalized neutrons have kinetic energies that are approximately equal to the energies of atoms constituting the scattering material. Thermalized neutrons have low velocities, and are readily absorbed by nuclei in the surrounding material. After neutrons are absorbed, two possibilities exist for what will happen next. Which of these two possibilities occurs depends on the circumstances of the nuclei and neutron system. Either the process ends there without release of any more neutrons, or there is a fission reaction and release of one or more neutrons.

Neutron Interactions

Neutrons may scatter off or be absorbed into target nuclei in a scattering material. Absorbed neutrons may cause the target nucleus to fission or emit a gamma ray or subatomic particle. Scattering occurs when an incident neutron strikes a target nucleus and a single neutron is emitted. The incident and scattered neutrons are not necessarily the same. Neutron scattering off the target nucleus can be an elastic or inelastic process. In elastic scattering, there is no energy transferred from the incident neutron to nuclear excitation. Total kinetic energy and momentum of the neutron and nucleus system remain constant during the collision and are conserved quantities. During elastic scattering of an incident neutron off of a target nucleus, it is possible that some kinetic energy may transfer from the neutron to the target nucleus causing the nucleus to recoil. This process is illustrated in Figure 1.

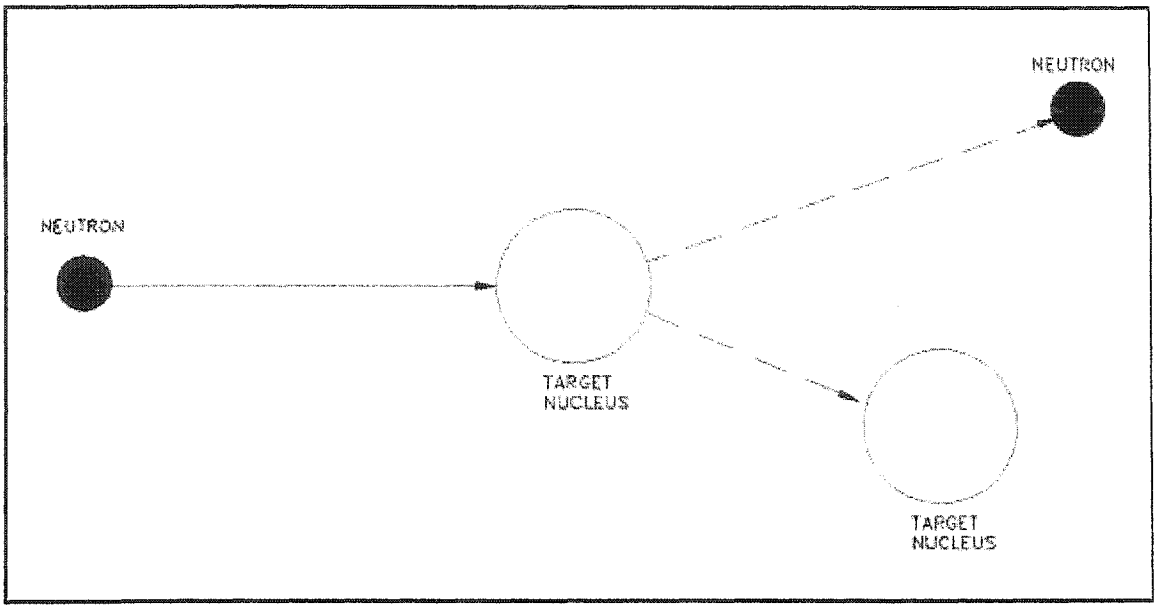

Fig. 1. Neutron elastic scattering off of a target nucleus.

Two different processes may occur during elastic scattering. The less common process is when an incident neutron is absorbed into a target nucleus forming a compound nucleus. The compound nucleus is left in an excited state, but it quickly emits a neutron having the right amount of kinetic energy to return the excited nucleus to its ground state. This process is called resonance or compound elastic scattering and it depends greatly on the kinetic energy of the incident neutron. The more common process is called potential elastic scattering. Potential elastic scattering happens when an incident neutron has energy of about 1 MeV. During the collision, a neutron is scattered by short-range nuclear forces, and no compound nucleus is formed. Potential elastic scattering requires an incident neutron to come within close proximity of a target nucleus so short-range nuclear forces may come into play. As is the case for resonance elastic scattering, inelastic scattering occurs when an incident neutron is absorbed by a target nucleus, forming a compound nucleus. In inelastic scattering, the excited nucleus emits a neutron

having less kinetic energy than that of the incident neutron, thereby leaving the nucleus in an excited state. Through the subsequent emission of gamma rays, the excited nucleus usually returns to its ground state. Figure 2 illustrates the inelastic scattering process.

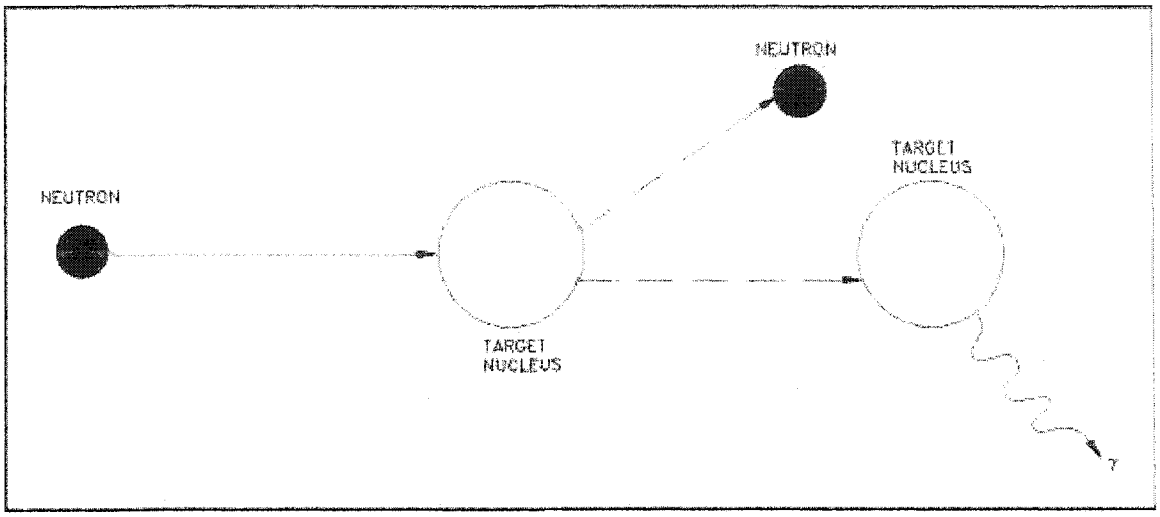

Fig. 2. Neutron inelastic scattering off of a target nucleus.

If the target nucleus returns to its ground state then the sum of the scattered neutron and target nucleus kinetic energies plus the total energy of the emitted gamma ray equals the kinetic energy of the incident neutron.

Absorption of an incident neutron by a target nucleus usually brings about emission of a charged particle, neutron, or gamma ray from the nucleus. There are three types of absorption processes. These processes are radiative capture, particle ejection, and fission. In radiative capture, a compound nucleus forms when an incident neutron is absorbed by a target nucleus. The compound nucleus emits a gamma ray and returns to its ground state. In particle ejection, an incident neutron is absorbed by a target nucleus, forming a compound nucleus. The compound nucleus is in a highly excited state and

proceeds to eject a new particle (for example a proton or alpha particle) while the incident neutron remains inside the nucleus. After the new particle is ejected, the nucleus may return to its ground state. Fission is when a target nucleus absorbs an incident neutron, and the nucleus proceeds to split into two pieces of approximately the same size. Neutrons that are produced by fission have energies that usually range from 0.1 to 10 MeV. Plotting the fraction of neutrons produced by fission per MeV as a function of neutron energy generates a fission neutron energy spectrum. Figure 3 is the fission neutron energy spectrum for Uranium 235. Neutrons having energy of about 0.7 MeV are the most probable to be found in the figure.

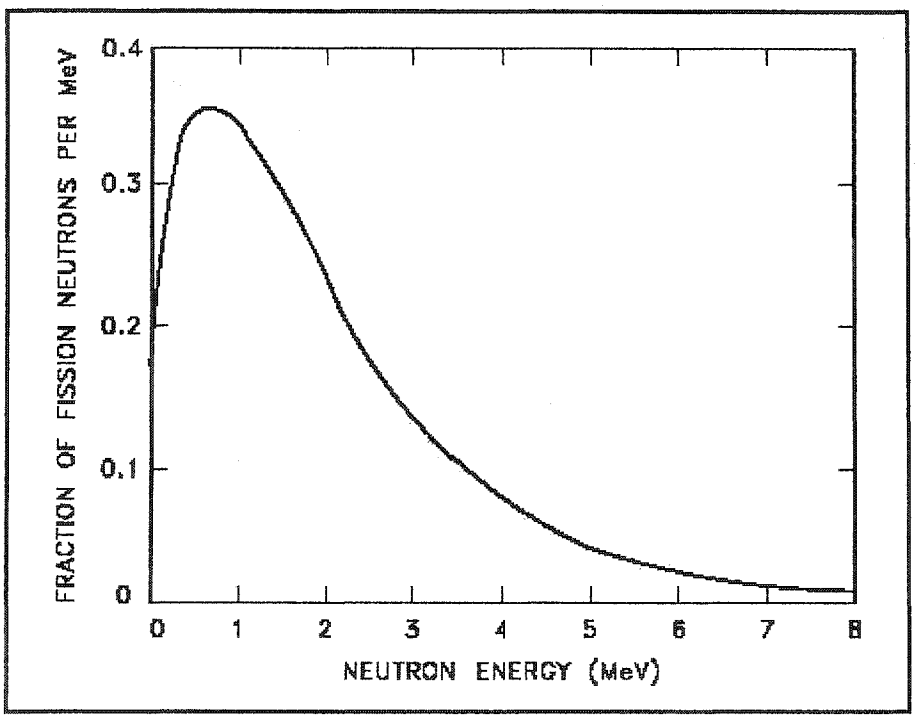

Fig. 3. Fission neutron energy spectrum for uranium 235.

Neutrons scattered in the forward direction are often referred to as direct knock out or cascading neutrons. Direct knockout neutrons result when incident neutrons collide with target nuclei and transfer their energy and momentum to neutrons in the nuclei. To conserve momentum and energy, target nuclei release neutrons that travel in approximately the forward direction. The forward-backward model is used to compute only isotropic evaporation neutrons. Evaporation neutrons are produced when incident neutrons collide with target nuclei. The collisions cause target nuclei to transition into an excited state, and shortly thereafter return to a more stable configuration by ejecting neutrons isotropically. Let $f^{e}_{n,n}(E,E')$ represent the number of evaporation neutrons per MeV having energy E that are produced in a material slab from incident neutrons with energy E', and let $f^{d}_{n,n}(E,E')$ represent the number of direct knock out neutrons per MeV having energy E that are produced in a material slab from incident neutrons with energy E'. The relationship between $f^{e}_{n,n}(E,E')$ and $f^{d}_{n,n}(E,E')$ is illustrated in Figure 4 for 500 MeV neutrons incident on an aluminum slab[13]. Evaporation neutrons dominate at energies less than 20 MeV, and direct knockout neutrons dominate at higher energies.

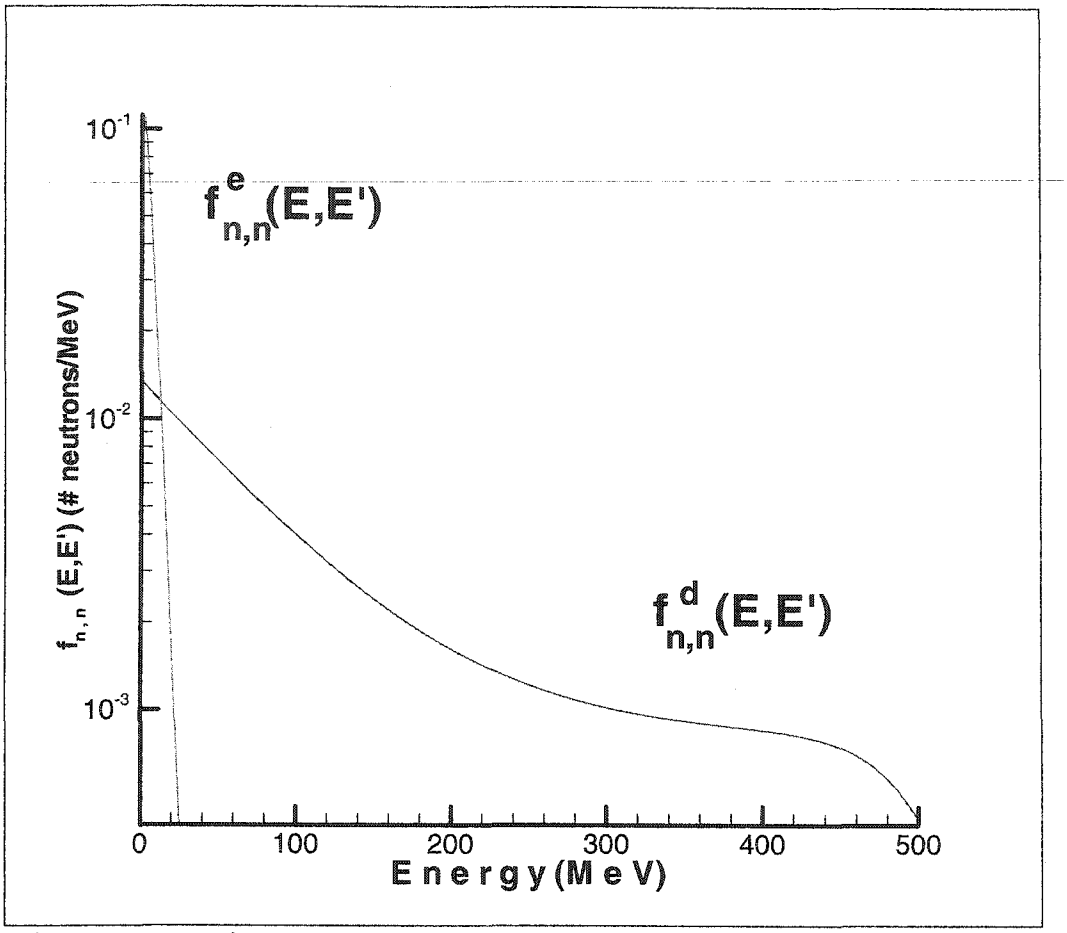

Fig. 4. Evaporation and cascading neutron effects for the collision of 500 MeV neutrons in an aluminum slab.

Flux and Fluence

To determine the number of interactions neutrons undergo as they pass through a slab of material, it is necessary to know the number of neutrons traveling through the material and how many centimeters they advance each second. It is useful to consider the number of neutrons residing in a cubic centimeter of material at a given moment, and the distance they travel per second while in the volume. Neutron density is defined as the number of neutrons located in a cubic centimeter of material at any instant. Neutron flux is the number of neutrons per unit area and time that are falling on a surface

perpendicular to the direction of the incident neutron beam. The relationship between neutron flux, neutron density, and average neutron velocity is given by

$$\Phi = nV, \tag{2.1}$$

where

$$\begin{aligned} \Phi &= \text{neutron flux}\left(\frac{\#\text{ of neutrons}}{\text{cm}^2 - \text{sec}}\right), \\ n &= \text{neutron density}\left(\frac{\#\text{ of neutrons}}{\text{cm}^3}\right), \text{ and} \\ V &= \text{average neutron velocity}\left(\frac{\text{cm}}{\text{sec}}\right). \end{aligned} \tag{2.2}$$

Neutrons travel in all directions in a material slab. This makes it difficult to compute neutron flux in materials, and frequently approximations must be made in order to make the computations more tractable. If the material slab is in a state of equilibrium that is not changing over time, it is useful to consider how the number of neutrons passing through a unit area varies with neutron energy. The quantity that describes this relationship is called neutron fluence, and has units $\left(\frac{\#\text{ of neutrons}}{\text{cm}^2 - \text{MeV}}\right)$.

Cross Sections

To compute neutron fluence in a material slab it is important to know what the probability is for a neutron to interact with a nucleus. The probability depends on the incident neutron's energy and the type of target nucleus involved in the interaction. It is more probable for slower moving thermal neutrons to be absorbed by target nuclei than it is for faster moving neutrons. Microscopic cross section refers to the probability of a

particular type of reaction to occur between a neutron and nucleus and is a function of neutron energy. One can think of microscopic cross section as being the effective area a nucleus makes available to an incident neutron for a particular type of interaction to occur. As the effective area increases, the probability for that particular interaction to occur becomes larger. Microscopic cross sections have area units, such as cm^2. The effective area of a nucleus is much smaller than a square centimeter, and a smaller unit of measurement called a barn is used when referring to nuclear processes. The conversion between a barn and square centimeter is

$$1 \text{ barn} = 10^{-24} \text{ cm}^2. \tag{2.3}$$

Neutrons interact with atoms in a material through scattering processes or by absorption. Let σ_a represent the microscopic cross section for a neutron to be absorbed by a particular atom, and σ_s represent the microscopic cross section for a neutron to scatter off of a particular nucleus. Table II gives σ_a and σ_s for thermal neutrons in aluminum and silicon.

Table II
Absorption and Scattering Microscopic Cross Sections for Thermal Neutrons.

Element	Gram Atomic Weight	$\sigma_{a\,(barns)}$	$\sigma_{s\,(barns)}$
Aluminum	26.9815	0.23	1.49
Silicon	28.0855	0.16	2.20

The total microscopic cross section σ_T is the sum of the absorption and scattering microscopic cross sections, and is given by

$$\sigma_T = \sigma_a + \sigma_s. \tag{2.4}$$

Microscopic scattering cross sections are the sum of elastic and inelastic scattering cross sections. Microscopic absorption cross sections represent all types of interactions other than scattering. It is common practice to separate microscopic absorption cross sections into fission and capture classifications. Fission is not applicable to shielding materials.

Absorption cross sections depend on incident neutron energy. For many elements, when incident neutrons are slow, absorption cross sections range from a fraction of a barn up to a few barns. Figure 5, taken from reference [12], illustrates general features of a typical neutron absorption cross section plotted as a function of neutron energy.

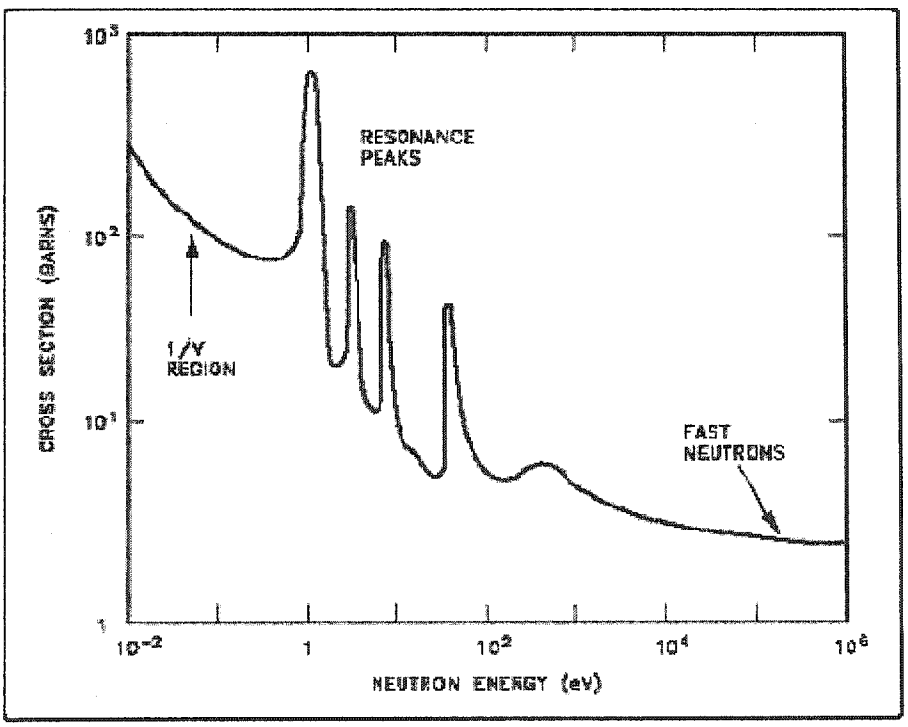

Fig. 5. Typical neutron absorption cross section versus neutron energy.

In the low-energy region the absorption cross section decreases with increasing neutron energy. The low-energy region is characterized by energies less than 0.75 eV, and includes slow thermal neutrons. The absorption cross section in the low-energy region is inversely proportional to neutron velocity V. Therefore, this is referred to as the 1/V region. Since thermal neutrons move slowly in the low-energy range; the absorption cross section is large.

The resonance region follows the 1/V region as neutron energy increases. Sharp resonance peaks exist in the resonance region. Resonance peaks occur when incident neutron energies are equal to a quantum energy level of the target nucleus. To be more precise, a resonance absorption peak occurs when the sum of the binding and kinetic energies of the incident neutron equals the amount of energy needed to raise the compound nucleus from its ground state to a higher quantum energy level. A heavy nucleus will usually have many resonance absorption peaks in the low-energy region. These resonances can be attributed to heavy nuclei having many energy states. On the other hand, light nuclei have less complicated structures than heavy nuclei. The relative simplicity in structure results in light nuclei having fewer energy states and absorption resonance peaks than heavy nuclei.

Absorption cross sections decrease as neutron energy increases beyond the resonance peaks region. The high-energy region where neutron energy is greater than 10^3 eV is called the fast neutron region. In this region, neutron absorption cross sections are typically less than 10 barns. It is of interest to compare neutron absorption cross sections in this region with the 5 to 10 barns range of elastic scattering cross sections that exist for all elements except hydrogen, which has a larger value. Geometric cross

sectional area of atomic nuclei also ranges from about 5 to 10 barns. It should be noted that, in general, there are more variations in absorption than in scattering cross sections.

The question arises if a neutron will interact with a volume of material. A measure of whether an interaction will proceed is determined by multiplying the microscopic cross section of a single target nucleus by the number of nuclei present in a volume of material along the neutron's trajectory. Macroscopic cross section is defined as the probability for a specific interaction to occur per unit length of travel by an incident neutron. Macroscopic and microscopic cross sections are related by the equation

$$\Sigma = N\sigma, \tag{2.5}$$

where

$$\begin{aligned} \Sigma &= \text{macroscopic cross section} \left(\frac{1}{\text{cm}}\right), \\ N &= \text{atomic density of a material} \left(\frac{\#\text{ of atoms}}{\text{cm}^3}\right), \text{ and} \\ \sigma &= \text{microscopic cross section} \left(\text{cm}^2\right). \end{aligned} \tag{2.6}$$

The atomic density of a material is computed by multiplying the density $\left(\frac{\text{grams}}{\text{cm}^3}\right)$ by Avogadro's number $\left(\frac{6.022\times10^{23}\text{ atoms}}{\text{mole}}\right)$ and dividing by the atomic weight $\left(\frac{\text{grams}}{\text{mole}}\right)$.

The microscopic cross section is a measure of the effective target area a single nucleus presents to an incident neutron. The macroscopic cross section is a measure of the effective target area presented by all nuclei contained in a cubic centimeter of material to an incident neutron.

CHAPTER III

THEORY

The neutron transport equation is also called the Boltzmann equation because it is similar to the expression developed by L. Boltzmann describing the kinetic theory of gases. Researchers at NASA Langley Research Center are interested in finding the distribution of neutrons in various materials as a function of depth and neutron energy. Monte Carlo statistical methods substitute material cross sections (i.e. neutron interaction probabilities) into the neutron transport equation to compute neutron distributions. Monte Carlo methods are very computer resource intensive, requiring long periods of time to complete computations. The forward-backward deterministic model developed in chapter IV also uses cross sections to compute neutron distributions in materials, but requires much less computer time to reach the solution. Since material cross sections and their dependence on neutron energy are not completely known, computational errors due to uncertainties in cross sections are sure to be present. In the next section, the neutron transport equation is derived using reference [14] as a guide.

Derivation of the Neutron Transport Equation

Let $N(\boldsymbol{r}, \boldsymbol{\Omega}, E, t)\, dV\, d\boldsymbol{\Omega}\, dE$ represent the number of neutrons at time t that are located in a volume element dV with energies in a range from E to $E + dE$, and are moving in directions within a narrow beam $d\boldsymbol{\Omega}$ about the direction $\boldsymbol{\Omega}$. Figure 6 illustrates the relationship between the volume element dV and direction $\boldsymbol{\Omega}$.

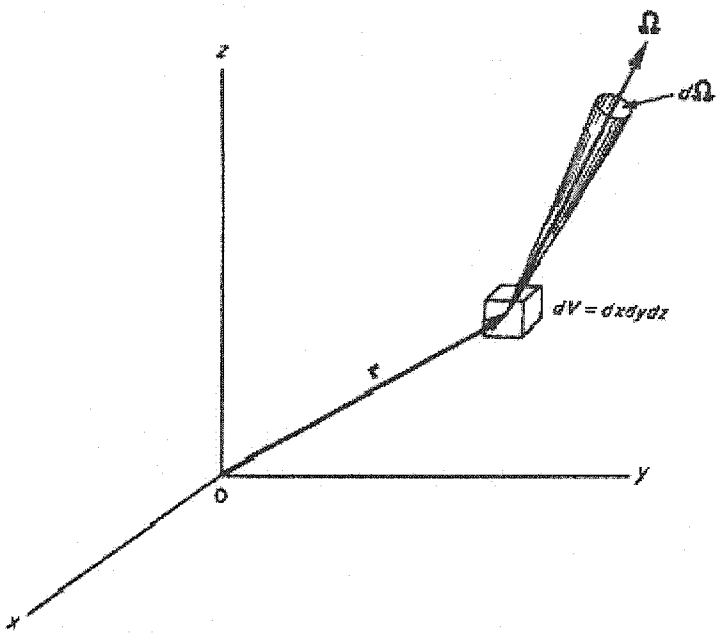

Fig. 6. The volume element dV and direction $\mathbf{\Omega}$.

Cross sections are continuous functions of position $\boldsymbol{r}$ in a single material. For two materials, cross sections change discontinuously across the boundary interface separating them. Consider a "packet" of neutrons located within a single material. Neutrons having energy E before a collision lose energy during the collision and have energy less than E after the collision. These neutrons are no longer in the packet. Neutrons remain in the packet if they do not undergo a collision. A neutron moving at a constant speed v will travel distance $v\Delta t$ in time Δt. Let $\sigma(\boldsymbol{r}, E)$ represent the total cross section of the material. The probability that a neutron will undergo a collision during the time Δt is $\sigma(\boldsymbol{r}, E)\, v\Delta t$ to first order in Δt. The probability a neutron will not experience a collision during the time Δt and stay in the packet is $1 - \sigma(\boldsymbol{r}, E)\, v\Delta t$. The number of neutrons remaining in the packet is given by

$$N(\boldsymbol{r}, \mathbf{\Omega}, E, t)\,[1 - \sigma(\boldsymbol{r}, E)\, v\Delta t]\, dV\, d\mathbf{\Omega}\, dE. \tag{3.1}$$

These neutrons will move from position $\boldsymbol{r}$ at time t to position $\boldsymbol{r} + \boldsymbol{\Omega} v \Delta t$ at time $t + \Delta t$.

If neutrons outside of the packet undergo a collision, some of them may enter the packet. The number of neutrons entering the packet as a result of collisions is given by

$$\left[\iint \sigma(\boldsymbol{r}, E') f(\boldsymbol{r}; \boldsymbol{\Omega}', E' \rightarrow \boldsymbol{\Omega}, E)\, v' N(\boldsymbol{r}, \boldsymbol{\Omega}', E', t)\, d\boldsymbol{\Omega}'\, dE'\right] dV\, d\boldsymbol{\Omega}\, dE\, \Delta t. \qquad (3.2)$$

In expression (3.2), $f(\boldsymbol{r}; \boldsymbol{\Omega}', E' \rightarrow \boldsymbol{\Omega}, E)$ represents the probability for a neutron moving in direction $\boldsymbol{\Omega}'$ with energy E' to scatter into a cone $d\boldsymbol{\Omega}$ about direction $\boldsymbol{\Omega}$ with energy between E and $E + dE$. Inside the material, there could be sources of neutrons. The number of neutrons entering the packet from sources is given by

$$Q(\boldsymbol{r}, \boldsymbol{\Omega}, E, t)\, dV\, d\boldsymbol{\Omega}\, dE\, \Delta t. \qquad (3.3)$$

In expression (3.3), $Q(\boldsymbol{r}, \boldsymbol{\Omega}, E, t)$ represents the number of source term neutrons at position $\boldsymbol{r}$ that are moving in the direction $\boldsymbol{\Omega}$ with energy E at time t.

Adding expressions (3.1), (3.2), and (3.3) and dividing by $dV\, d\boldsymbol{\Omega}\, dE$ gives the neutron angular density at position $\boldsymbol{r} + \boldsymbol{\Omega} v \Delta t$ at time $t + \Delta t$, namely

$$N(\boldsymbol{r} + \boldsymbol{\Omega} v \Delta t, \boldsymbol{\Omega}, E, t + \Delta t) = N(\boldsymbol{r}, \boldsymbol{\Omega}, E, t)\,[1 - \sigma(\boldsymbol{r}, E)\, v \Delta t]$$

$$+ \left[\iint \sigma(\boldsymbol{r}, E') f(\boldsymbol{r}; \boldsymbol{\Omega}', E' \rightarrow \boldsymbol{\Omega}, E)\, v' N(\boldsymbol{r}, \boldsymbol{\Omega}', E', t)\, d\boldsymbol{\Omega}'\, dE'\right] \Delta t$$

$$+ Q \Delta t. \qquad (3.4)$$

Equation (3.4) is simplified by substituting $\sigma = \sigma(\boldsymbol{r}, E)$, $Q = Q(\boldsymbol{r}, \boldsymbol{\Omega}, E, t)$, and $\sigma' f = \sigma(\boldsymbol{r}, E') f(\boldsymbol{r}; \boldsymbol{\Omega}', E' \rightarrow \boldsymbol{\Omega}, E)$ into the expression. The simpler looking expressing takes the form

$$N(\boldsymbol{r} + \boldsymbol{\Omega} v \Delta t, \boldsymbol{\Omega}, E, t + \Delta t) = N(\boldsymbol{r}, \boldsymbol{\Omega}, E, t)\,(1 - \sigma v \Delta t)$$

$$+ \left[\iint \sigma' f\, v' N(\boldsymbol{r}, \boldsymbol{\Omega}', E', t)\, d\boldsymbol{\Omega}'\, dE'\right] \Delta t + Q \Delta t. \qquad (3.5)$$

Dividing both sides of equation (3.5) by Δt, and letting $\Delta t \to 0$ gives

$$\lim_{\Delta t \to 0}\left[\frac{N(\boldsymbol{r}+\boldsymbol{\Omega} v\Delta t, \boldsymbol{\Omega}, E, t+\Delta t) - N(\boldsymbol{r}, \boldsymbol{\Omega}, E, t)}{\Delta t}\right] + \sigma v N(\boldsymbol{r}, \boldsymbol{\Omega}, E, t)$$

$$= \iint \sigma' f v' N(\boldsymbol{r}, \boldsymbol{\Omega}', E', t)\, d\boldsymbol{\Omega}'\, dE' + Q. \tag{3.6}$$

The first term on the left hand side of equation (3.6) represents the time derivative of neutron angular density.

Now add and subtract $N(\boldsymbol{r}, \boldsymbol{\Omega}, E, t+\Delta t)$ to the numerator in square brackets in equation (3.6). This gives rise to two expressions, the first being

$$\lim_{\Delta t \to 0}\left[\frac{N(\boldsymbol{r}, \boldsymbol{\Omega}, E, t+\Delta t) - N(\boldsymbol{r}, \boldsymbol{\Omega}, E, t)}{\Delta t}\right] = \frac{\partial N}{\partial t}. \tag{3.7}$$

The second expression is arrived at by first referring to a Cartesian coordinate system where $\boldsymbol{r}$ has components x, y, z; $\boldsymbol{\Omega}$ has components $\boldsymbol{\Omega}_x, \boldsymbol{\Omega}_y, \boldsymbol{\Omega}_z$; and N has the functional dependence $N(x, y, z\ldots)$. This gives

$$\lim_{\Delta t \to 0}\left[\frac{N(x+\boldsymbol{\Omega}_x v\Delta t, y+\boldsymbol{\Omega}_y v\Delta t, z+\boldsymbol{\Omega}_z v\Delta t, \ldots) - N(x, y, z, \ldots)}{\Delta t}\right]$$

$$= v\boldsymbol{\Omega}_x \frac{\partial N}{\partial x} + v\boldsymbol{\Omega}_y \frac{\partial N}{\partial y} + v\boldsymbol{\Omega}_z \frac{\partial N}{\partial z}. \tag{3.8}$$

The second expression is obtained by writing equation (3.8) in vector form as

$$\lim_{\Delta t \to 0}\left[\frac{N(r+\Omega v\Delta t,\Omega,E,t+\Delta t)-N(r,\Omega,E,t+\Delta t)}{\Delta t}\right]=v\Omega\cdot\nabla N(r,\Omega,E,t). \quad (3.9)$$

Substituting equations (3.7) and (3.9) in equation (3.6) gives

$$\frac{\partial N}{\partial t}+v\Omega\cdot\nabla N(r,\Omega,E,t)+\sigma vN(r,\Omega,E,t) = \iint\sigma' fv' N(r,\Omega',E',t)\,d\Omega'\,dE'+Q. \quad (3.10)$$

Using the definitions given above for σ, σ′ f, and Q; letting $N = N(r,\Omega,E,t)$ and $N' = N(r,\Omega',E',t)$ yields the simpler appearing expression

$$\frac{\partial N}{\partial t}+ v\Omega\cdot\nabla N+\sigma vN = \iint\sigma' fv' N'\,d\Omega'\,dE'+Q. \quad (3.11)$$

Equation (3.11) is the neutron transport equation. The first term on the left hand side of equation (3.11) represents the time rate of change of neutron angular density at fixed location r. The second term on the left hand side of the equation is called the streaming term, and represents the neutrons moving in a straight line without experiencing any collisions.

The neutron transport equation can be expressed in terms of the angular flux Φ. Letting $\Phi = vN = \Phi(r,\Omega,E,t)$ and $\Phi' = v'N' = \Phi(r,\Omega',E',t)$, equation (3.11) becomes

$$\frac{1}{v}\cdot\frac{\partial\Phi}{\partial t}+ \Omega\cdot\nabla\Phi+\sigma\Phi = \iint\sigma' f\Phi'\,d\Omega'\,dE'+Q. \quad (3.12)$$

Assuming a steady state condition, the angular flux Φ is independent of time. This simplification gives the steady state neutron transport equation

$$\Omega \cdot \nabla \Phi + \sigma \Phi = \iint \sigma' f \Phi' \, d\Omega' \, dE' + Q. \tag{3.13}$$

To further simplify the problem only the x spatial dimension is used. Therefore, it is not necessary to integrate over incident directions Ω' and energies E' in equation (3.13). Only integration over incident neutron energy E' is needed to compute the number of neutrons moving in the specified direction with scattered energy E at depth x, as shown in reference [12]. With this in mind and explicitly putting in variable dependences, equation (3.13) takes the form

$$\Omega_x \frac{\partial \Phi(x,E)}{\partial x} + \sigma(E)\Phi(x,E) = \int \sigma(E') f(E) \Phi(x,E') dE' + Q(x,E). \tag{3.14}$$

Letting $\mu = \Omega_x$ and $f(E,E') = \sigma(E') f(E)$ in equation (3.14) gives

$$\mu \frac{\partial \Phi(x,E)}{\partial x} + \sigma(E)\Phi(x,E) = \int f(E,E')\Phi(x,E') dE' + Q(x,E). \tag{3.15}$$

The function $f(E,E')$ represents the probability a neutron having incident energy E' undergoes a collision and scatters with new energy E. This function dependends on the type of element doing the scattering, and the integral must be summed over all the different elements in the material. Accounting for this fact changes equation (3.15) into

$$\mu\frac{\partial\Phi(x,E)}{\partial x}+\sigma(E)\Phi(x,E)=\sum_m\int f_m(E,E')\Phi(x,E')dE'+Q(x,E), \qquad (3.16)$$

where m runs over the number of different elements in the material. The limits of integration and value of μ are evaluated in the next section of this chapter.

The first term on the left hand side of equation (3.16) represents the change in neutron fluence with a change in depth in the material. The second term on the left hand side represents the loss of neutrons due to absorption processes. The first term on the right hand side represents the gain in neutrons produced as secondaries in collisions having energy E at depth x in the material. Finally, the second term on the right hand side of equation (3.16) represents the gain in neutrons from sources in the material. With some modification, as shown below, equation (3.16) is put into the form of the neutron transport equation used in the forward-backward model.

The HZETRN Code

The HZETRN code developed at NASA Langley Research Center is used to solve the Boltzmann transport equation of the form

$$\begin{aligned}&\boldsymbol{\Omega}\cdot\nabla\boldsymbol{\Phi}_j(\boldsymbol{x},\boldsymbol{\Omega},E)-\frac{\partial}{\partial E}[S_j(E)\boldsymbol{\Phi}_j(\boldsymbol{x},\boldsymbol{\Omega},E)]\\&=\sum_k\int\sigma_{jk}(\boldsymbol{\Omega},\boldsymbol{\Omega}',E,E')\boldsymbol{\Phi}_k(\boldsymbol{x},\boldsymbol{\Omega}',E')d\boldsymbol{\Omega}'dE'-\sigma_j(E)\boldsymbol{\Phi}_j(\boldsymbol{x},\boldsymbol{\Omega},E).\end{aligned} \qquad (3.17)$$

In equation (3.17), the symbol $\boldsymbol{\Phi}_j(\boldsymbol{x},\boldsymbol{\Omega},E)$ represents the flux density of type j particles moving in direction $\boldsymbol{\Omega}$ with energy E at depth x in a material slab. The quantity $\sigma_j(E)$ represents the media macroscopic cross section for removal of type j particles having

energy E from the flux density. The term $S_j(E)$ represents the stopping power of type j particles having energy E in the material, and $\sigma_{jk}(\Omega, \Omega', E, E')$ represents the media macroscopic cross section for various atomic and nuclear scattering processes. Scattering processes add to the flux density type j particles that are moving in the direction Ω with energy E.

Media macroscopic cross sections are the cross sectional sums of particles scattered in the forward and isotropic directions. This relationship is expressed by the equation

$$\sigma_{jk} = \sigma_f + \sigma_{iso}. \tag{3.18}$$

In equation (3.18), σ_f represents the cross sections of particles scattered in the forward direction, and σ_{iso} represents the cross sections of isotropically scattered particles. Scattering in the forward direction refers to particles scattered through a small solid angle around the incident direction. In the low-energy range, $E < 100$ MeV, neutron scattering is dominated by the σ_{iso} term. In the high-energy range, $E \geq 100$ MeV, neutron scattering is dominated by the σ_f term.

The fluence Φ_j can be separated into a sum of forward Φ_j^F and isotropic Φ_j^{iso} directions, and expressed as

$$\Phi_j = \Phi_j^F + \Phi_j^{iso}. \tag{3.19}$$

The forward and isotropic directions are associated with high and low energies, respectively. Substituting equations (3.18) and (3.19) into equation (3.17) gives

$$\Omega \cdot \nabla(\Phi_j^F + \Phi_j^{iso}) - \frac{\partial}{\partial E}[S_j(E)(\Phi_j^F + \Phi_j^{iso})]$$
$$= \sum_k \int(\sigma_f + \sigma_{iso})(\Phi_k^F + \Phi_k^{iso}) d\Omega' dE' - \sigma_j(E)(\Phi_j^F + \Phi_j^{iso}). \tag{3.20}$$

Summation on the right hand side of equation (3.20) is done over different particles transporting through the scattering material. The term $\sigma_f \Phi_k^{iso}$ can be neglected because forward scattering cross sections are very small for low-energy isotropic particles. Equation (3.20) becomes

$$\Omega \cdot \nabla(\Phi_j^F + \Phi_j^{iso}) - \frac{\partial}{\partial E}[S_j(E)(\Phi_j^F + \Phi_j^{iso})]$$
$$= \sum_k \int(\sigma_f \Phi_k^F + \sigma_{iso}\Phi_k^F + \sigma_{iso}\Phi_k^{iso}) d\Omega' dE' - \sigma_j(E)(\Phi_j^F + \Phi_j^{iso}). \tag{3.21}$$

The HZETRN code can be used to solve the equation

$$\Omega \cdot \nabla \Phi_j^F - \frac{\partial}{\partial E}[S_j(E)\Phi_j^F] = \sum_k \int \sigma_f \Phi_k^F d\Omega' dE' - \sigma_j(E)\Phi_j^F \tag{3.22}$$

for the forward fluence Φ_j^F. Set $S_j(E) = 0$ for neutrons because they are electrically neutral particles. The low-energy isotropic neutron fluence is obtained by solving

$$\Omega \cdot \nabla \Phi_j^{iso} + \sigma_j(E)\Phi_j^{iso} = \sum_k \int \sigma_{iso} \Phi_k^{iso} d\Omega' dE' + Q(x, E), \tag{3.23}$$

where

$$Q(x, E) = \sum_k \int \sigma_{iso}(\Omega, \Omega', E, E') \Phi_k^F(x, \Omega', E') d\Omega' dE'. \tag{3.24}$$

In equations (3.23) and (3.24), $Q(x,E)$ represents a source of isotropic neutrons having energy E at depth x. These isotropic neutrons are produced by the interactions of forward moving particles with target nuclei, and can be computed using the HZETRN code. Equation (3.22) describes the production of energetic forward scattered particles in a material slab being bombarded by a beam of incident particles. Equation (3.23) describes the production of less energetic isotropically scattered neutrons. The source term generated by the HZETRN code at NASA Langley Research Center is used as input in the forward-backward model.

Neutrons scattered in the laboratory frame of reference between 0 and $\frac{\pi}{2}$ radians are considered scattered in the forward direction in the straight-ahead approximation of isotropic neutron fluence. Neutrons scattered between $\frac{\pi}{2}$ and π radians are considered scattered in the backward direction. This approximation reduces equation (3.23) to one spatial dimension and is written as

$$\mu\frac{\partial\Phi(x,E)}{\partial x}+\sigma(E)\Phi(x,E)=\sum_m\int_E^{E/\alpha_m} f_m(E,E')\Phi(x,E')dE'+Q(x,E), \qquad (3.25)$$

where

$$\mu=\begin{Bmatrix}\cos(0)=+1 & \text{for the forward direction, or}\\ \cos(\pi)=-1 & \text{for the backward direction.}\end{Bmatrix} \qquad (3.26)$$

Summation on the right hand side of equation (3.25) is done over different nuclei constituting the scattering material. In equation (3.25), $f_m = f_m(E,E')$ are elastic

scattering terms, $\Phi(x, E)$ represents the steady state fluence of evaporation neutrons at depth x having energy E, and $\sigma(E) = \sum_m \rho_m \sigma_m^{el}(E)$ is the isotropic cross section. The quantity ρ_m represents the number of atoms per gram of slab material and $\sigma_m^{el}(E)$ represents the microscopic elastic scattering cross section for the mth type of atom. The limits of integration in equation (3.25) are obtained by considering the elastic scattering of a neutron off of a nucleus that is initially at rest. The equation

$$E = E'\left[\frac{A_{T_m}^2 + 2A_{T_m}\cos\theta_{CM} + 1}{(A_{T_m} + 1)^2}\right] \tag{3.27}$$

was taken from reference [15], and gives a relation between incident and scattered neutron energies E' and E, respectively. Here A_{T_m} is the atomic weight of the mth type of atom being bombarded by the flux density and θ_{CM} represents scattering angle in the center of mass frame of reference. The term signifying production of neutrons in equation (3.25) requires summation over all types of elements constituting the material slab, and denoted using summation index m. The laboratory and center of mass scattering angles are related by the transformation equation

$$\theta_{CM} = \theta_L + \arcsin\left(\frac{1}{A_T}\sin\theta_L\right), \tag{3.28}$$

where θ_L represents the laboratory scattering angle.

Figure 7 illustrates neutron scattering angle measured in the laboratory and center of mass frames of reference[15].

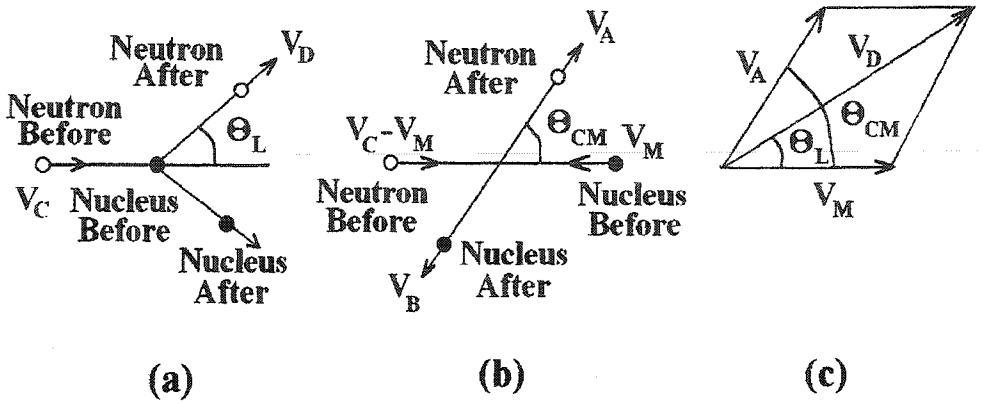

Fig. 7. (a) Laboratory system *L*. (b) Center of mass system *CM*. (c) Transformation from center of mass (*CM*) to laboratory system (*L*).

Minimum scattering occurs for $\theta_L = 0$ and $E = E'$, while maximum scattering occurs for $\theta_L = \pi$ and $E = E'\alpha_m$. The quantity α_m is given by

$$\alpha_m = \left(\frac{A_{T_m} - 1}{A_{T_m} + 1} \right)^2, \tag{3.29}$$

and is a constant whose value is less than one. The domain of integration is the energy interval $[E, E/\alpha_m]$ and represents the kinetically allowed energies for elastically scattered neutrons to be produced with energy *E*. This form of the equation has been investigated by Clowdsley and is included in the HZETRN code at NASA Langley Research Center[16–18].

The Space Radiation Environment

The space radiation environment consists mainly of energetic particles. Figure 8 illustrates that energetic particles are largely composed of atomic constituents, and the particle flux density of energetic particles varies with energy[1].

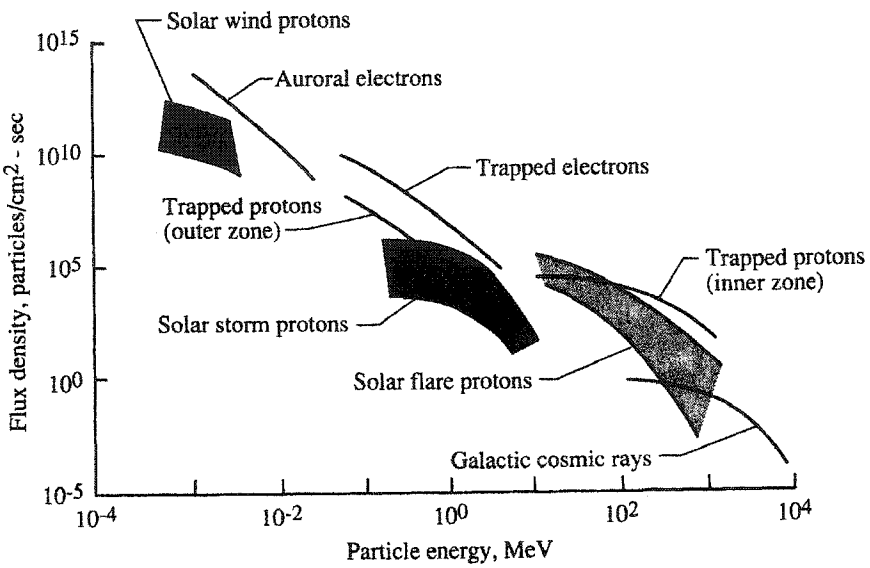

Fig. 8. The space radiation environment.

Particles in space are on the order of 10^{-13} centimeter in length and carry electric charge[1]. In a material slab, atomic electron clouds occupy nearly all the space, but constitute only 0.05 percent of the mass[1]. Atomic nuclei are 10^{-5} times smaller than the volume of the entire atom and make up 99.95 percent of the atomic mass[1]. An energetic particle traversing a material slab will mainly interact with electrons in the atomic electron clouds and seldom interact with atomic nuclei.

When a collision occurs between an incident energetic particle and atomic nucleus, a large fraction of the particle's kinetic energy is transferred to the nucleus. Large numbers of secondary particles are produced if a sufficient amount of kinetic energy is transferred. Energetic secondary particles are generated by various physical processes including the direct knockout of nuclear constituents, resonant excitation of nuclei followed by the emission of one or more particles, pair production, and possible coherent effects inside nuclei[1]. Which interaction process occurs depends on the incident particle's energy and type, and on the material composition of the slab. Figure 9 illustrates two cascading processes that occur in the Earth's atmosphere[1]. In the figure, a high-energy proton and alpha particle initiate cascading processes that result in the production of neutrons and protons. Similar processes occur when energetic particles pass through slabs of materials.

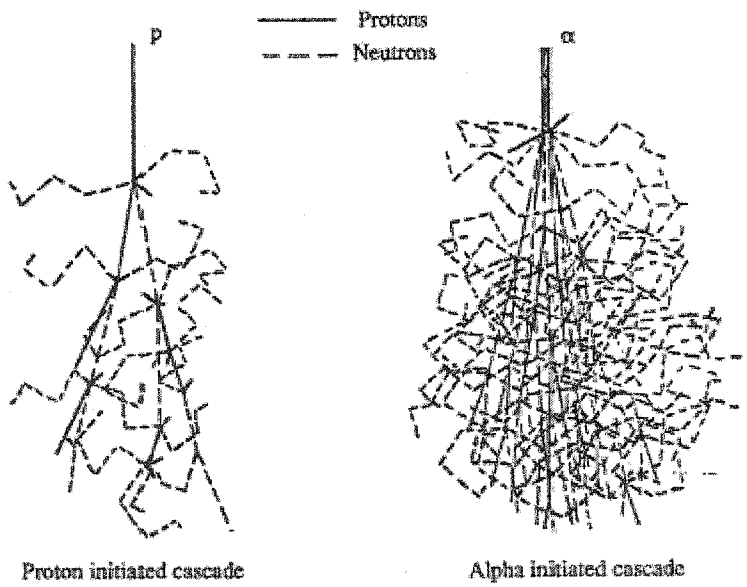

Fig. 9. The cascade process in the Earth's atmosphere.

Protons with energies less than 400 MeV mainly interact with electrons in any shield material[1]. Few incident protons collide with nuclei in a material slab before coming to a stop. Any nuclear collisions that occur do not produce many secondary particles. Trajectories of primary incident particles all reside within a small cylinder centered about the initial direction of motion. Any deviations from the initial direction of motion are attributed primarily to multiple scattering through small angles by coulomb forces. Collisions with nuclei become prevalent when incident particles have energies greater than or equal to several hundred MeV[1]. At these higher energies, most primary particles undergo nuclear collision before coming to a stop. Many secondary particles are produced, and the most energetic of them have trajectories lying in a narrow cone centered about the primary particle's direction of motion[1]. The trajectory cone becomes narrower as primary particle energy increases. Any secondary particles produced will probably have low energies. Charged low-energy secondary particles rapidly come to a stop at points very close to where they originated in the material. Low-energy secondary neutrons travel greater distances to points further away from the primary particle's direction of motion. Only an outward flux of low-energy neutrons exists at large distances from the primary particle's direction of motion. Low-energy neutron flux decreases exponentially as the distance from the primary particle's direction of motion increases[1]. The decrease in flux is due to neutron absorption in the material. High-energy primary particles, such as neutrons and protons, collide mainly with shield material nuclei and produce many secondary particles. Figure 10 illustrates the response in a material slab to a point source of monoenergetic protons moving along the *Z*-

direction. Low-energy neutrons form an elliptical shaped region having two foci lying along the Z-direction.

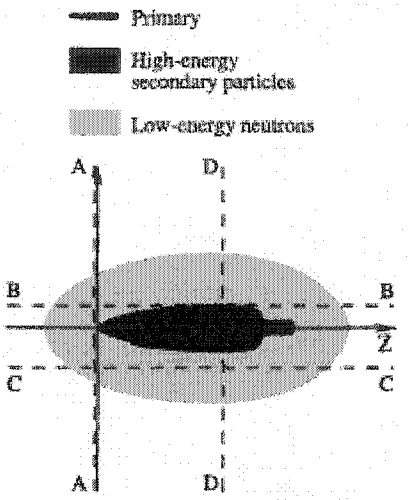

Fig. 10. Response to a point source of monoenergetic protons.

CHAPTER IV

THE MODEL

The form of the neutron transport equation used in the forward-backward fluence model is given by equation (3.16) with slight modifications. The limits of integration are determined from neutrons scattering off of target atoms through angle θ_L. The laboratory scattering angle θ_L is illustrated in Figure 11, where forward and backward neutron fluences are represented by ϕ_F and ϕ_B, respectively[13].

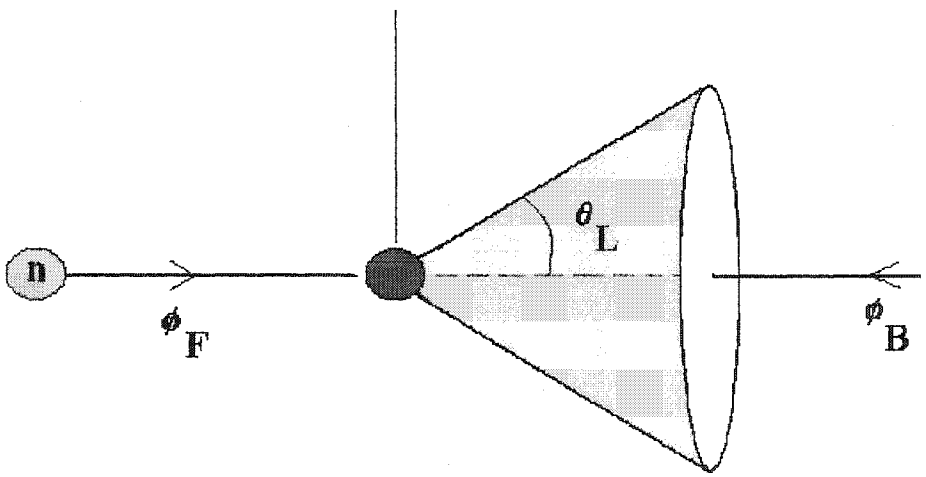

Fig. 11. Laboratory scattering angle.

Before discussing the scattering angle θ_L, it is useful to see an equation relating the neutron energy E after collision to both the energy E' before collision and the center of

mass scattering angle θ_{CM}. If A_T equals the atomic mass of atoms constituting the target material, then the equation alluded to in the previous sentence is given by

$$E = \frac{1}{2}E'[(1+\alpha)+(1-\alpha)\cos\theta_{CM}]. \tag{4.1}$$

The quantity α in equation (4.1) is less than 1, and given by the expression

$$\alpha = \left(\frac{A_T - 1}{A_T + 1}\right)^2. \tag{4.2}$$

The laboratory scattering angle θ_L is related to the center of mass scattering angle θ_{CM} by the transformation

$$\theta_{CM} = \theta_L + \sin^{-1}\left(\frac{1}{A_T}\sin\theta_L\right). \tag{4.3}$$

Angle θ_L must be between 0 and $\pi/2$ radians for neutrons to scatter in the forward direction. When $\theta_L = 0$, equation (4.3) gives $\theta_{CM} = 0$, and equation (4.1) gives $E = E'$. Define θ^*_{CM} to be the scattering angle when $\theta_L = \pi/2$. From equation (4.3) it follows

$$\theta^*_{CM} = \frac{\pi}{2} + \sin^{-1}\left(\frac{1}{A_T}\right). \tag{4.4}$$

Substituting equation (4.4) into equation (4.1), and defining α^* as

$$\alpha^* = \frac{1}{2}[(1+\alpha)+(1-\alpha)\cos\theta^*_{CM}] \tag{4.5}$$

gives the equation

$$E = \frac{1}{2}E'[(1+\alpha)+(1-\alpha)\cos\theta^*_{CM}] = E'\,\alpha^*. \tag{4.6}$$

Forward scattering occurs for incident neutron energies E' lying between E and E/α^*. Backward scattering occurs when θ_L is between $\pi/2$ and π radians. When $\theta_L = \pi$, equation (4.1) gives $E = E'\alpha$. Backward scattering occurs for incident neutron energies E' lying between E/α^* and E/α. As the scattering angle increases, higher incident neutron energy is needed to produce scattered neutrons having energy E.

The System of Equations

Incorporating the limits of integration into the neutron transport equation gives

$$\mu\frac{\partial\Phi(x,E)}{\partial x} + \sigma(E)\Phi(x,E) = \sum_m \int_E^{E/\alpha_m} f_m(E,E')\Phi(x,E')dE' + Q(x,E). \tag{4.7}$$

The total fluence $\Phi(x,E)$ is the sum of forward and backward fluence components $\Phi_F(x,E)$ and $\Phi_B(x,E)$, respectively, and is given by the equation

$$\Phi(x,E) = \Phi_F(x,E) + \Phi_B(x,E). \tag{4.8}$$

The source term $Q(x,E)$ is the sum of forward and backward components $Q_F(x,E)$ and $Q_B(x,E)$, respectively, and is given by the equation

$$Q(x,E) = Q_F(x,E) + Q_B(x,E). \tag{4.9}$$

It is assumed $Q_F(x,E) = Q_B(x,E) = \frac{1}{2}Q(x,E)$. Substituting equations (4.8) and (4.9) into equation (4.7) gives

$$\mu\frac{\partial}{\partial x}(\Phi_F + \Phi_B) + \sigma(E)(\Phi_F + \Phi_B) = \sum_m \int_E^{E/\alpha_m} f_m(E,E')(\Phi_F + \Phi_B)dE' + Q_F + Q_B. \tag{4.10}$$

The neutron scattering angle can be separated into forward and backward directions. The integral in equation (4.10) is separated into two integrals with appropriate limits of integration. The limits of integration were derived in the previous section, and are based on forward and backward scattering energy in the laboratory system. Equation (4.10) becomes

$$\mu\frac{\partial}{\partial x}(\Phi_F + \Phi_B) + \sigma(E)(\Phi_F + \Phi_B) = \sum_m \left[\int_E^{E/\alpha_m^*} f_m(E,E')(\Phi_F + \Phi_B)dE' + \int_{E/\alpha_m^*}^{E/\alpha_m} f_m(E,E')(\Phi_F + \Phi_B)dE' \right] + Q_F + Q_B. \tag{4.11}$$

It is assumed the forward fluence is governed by the equation

$$\mu\frac{\partial \Phi_F(x,E)}{\partial x} + \sigma(E)\Phi_F(x,E) = \sum_m \left[\int_E^{E/\alpha_m^*} f_m(E,E')\Phi_F(x,E')dE' + \int_{E/\alpha_m^*}^{E/\alpha_m} f_m(E,E')\Phi_B(x,E')dE' \right] + Q_F(x,E). \tag{4.12}$$

The backward fluence is therefore governed by the equation

$$\mu\frac{\partial\Phi_B(x,E)}{\partial x}+\sigma(E)\Phi_B(x,E)$$

$$=\sum_m\left[\int_E^{E/\alpha_m^*} f_m(E,E')\Phi_B(x,E')dE'+\int_{E/\alpha_m^*}^{E/\alpha_m} f_m(E,E')\Phi_F(x,E')dE'\right]+Q_B(x,E). \tag{4.13}$$

The variable x represents depth in the material, and extends from 0 to L. The boundary conditions imposed on the left and right edges of the material are

$$\Phi_F(0,E)=0 \tag{4.14}$$

and

$$\Phi_B(L,E)=0, \tag{4.15}$$

respectively. No low-energy isotropic neutrons enter the slab of material from external sources. A steady-state fluence of isotropic neutrons is created inside the material when bombarded by energetic particles.

Substituting the values for μ given in equation (3.26) into equations (4.12) and (4.13) gives

$$\frac{\partial\Phi_F(x,E)}{\partial x}+\sigma(E)\Phi_F(x,E)$$

$$=\sum_m\left[\int_E^{E/\alpha_m^*} f_m(E,E')\Phi_F(x,E')dE'+\int_{E/\alpha_m^*}^{E/\alpha_m} f_m(E,E')\Phi_B(x,E')dE'\right]+Q_F(x,E) \tag{4.16}$$

and

$$-\frac{\partial \Phi_B(x,E)}{\partial x}+\sigma(E)\Phi_B(x,E)$$

$$=\sum_m\left[\int_E^{E/\alpha_m^*} f_m(E,E')\Phi_B(x,E')dE'+\int_{E/\alpha_m^*}^{E/\alpha_m} f_m(E,E')\Phi_F(x,E')dE'\right]+Q_B(x,E), \tag{4.17}$$

respectively. It should be noted that elastic scattering terms $f_m(E,E')$ also depend on μ, and this dependence is written as $f_m(E,E',\mu)$. For the time being, neglect any dependence of the scattering terms on μ. A list of variables and corresponding units of measurement that are used in the forward-backward model are given in Appendix A.

The Collocation Solution

Assume solutions to the coupled system of equations (4.16) and (4.17) to be in the form of two series

$$\Phi_F(x,E)=\sum_{j=0}^{N}U_j(x)B_j(E)$$

and (4.18)

$$\Phi_B(x,E)=\sum_{j=0}^{N}V_j(x)B_j(E).$$

The functions $B_j(E)$ are linear splines having support $[E_{j-1},E_{j+1}]$. Define $B_j(E)$ as

$$B_j(E) = \begin{cases} \dfrac{E - E_{j-1}}{E_j - E_{j-1}} & \text{on } [E_{j-1}, E_j], \\ \dfrac{E_{j+1} - E}{E_{j+1} - E_j} & \text{on } [E_j, E_{j+1}], \\ 0 & \text{elsewhere.} \end{cases} \tag{4.19}$$

Linear B-splines have the property $B_j(E_j) = 1$, and are illustrated in Figure 12.

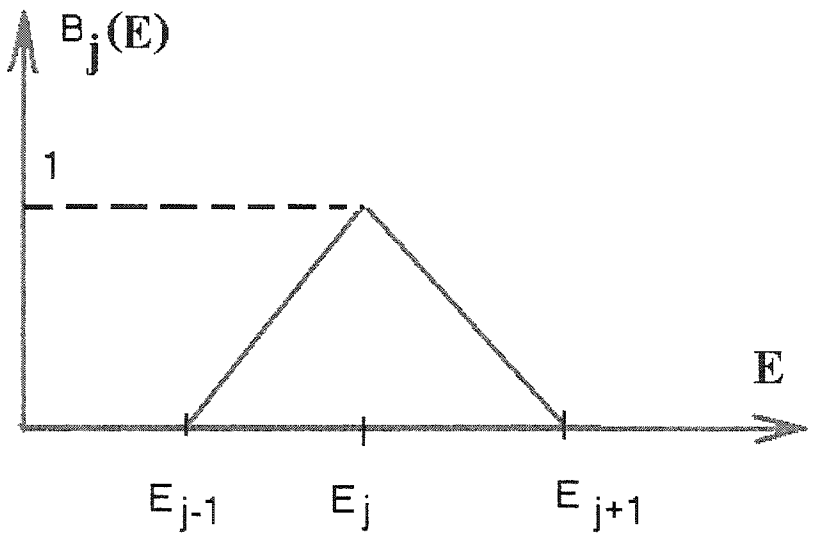

Fig. 12. Linear B-splines.

For the collocation method to work, the linear splines must be invertible and satisfy the condition $\det[B_j(E_i)] \neq 0$. Substituting assumed solutions (4.18) into equations (4.16) and (4.17) gives the coupled system of integro-differential equations

$$\sum_{j=0}^{N}\frac{\partial U_j}{\partial x}B_j(E)+\sum_{j=0}^{N}\sigma(E)U_jB_j(E)$$

$$=\sum_k\Big[\int_E^{E/\alpha_k^*}f_k(E,E')\sum_{j=0}^{N}U_jB_j(E')dE'+\int_{E/\alpha_k^*}^{E/\alpha_k}f_k(E,E')\sum_{j=0}^{N}V_jB_j(E')dE'\Big]+Q_F(x,E) \tag{4.20}$$

and

$$-\sum_{j=0}^{N}\frac{\partial V_j}{\partial x}B_j(E)+\sum_{j=0}^{N}\sigma(E)V_jB_j(E)$$

$$=\sum_k\Big[\int_E^{E/\alpha_k^*}f_k(E,E')\sum_{j=0}^{N}V_jB_j(E')dE'+\int_{E/\alpha_k^*}^{E/\alpha_k}f_k(E,E')\sum_{j=0}^{N}U_jB_j(E')dE'\Big]+Q_B(x,E). \tag{4.21}$$

Evaluate equations (4.20) and (4.21) at $E = E_i$, where $i = 0, 1, 2, \ldots, N$ and $0 \le x \le L$. At the left boundary impose the condition $U_i(0) = 0$, and at the right boundary impose $V_i(L) = 0$. Using $B_j(E_i) = 0$ for $i \ne j$ and $B_i(E_i) = 1$ gives the coupled system of ordinary differential equations

$$\frac{dU_i}{dx}+\sigma(E_i)U_i=\sum_{j=0}^{N}a_{ij}U_j+\sum_{j=0}^{N}b_{ij}V_j+Q_F(E_i,x)$$

and (4.22)

$$-\frac{dV_i}{dx}+\sigma(E_i)V_i=\sum_{j=0}^{N}b_{ij}U_j+\sum_{j=0}^{N}a_{ij}V_j+Q_B(E_i,x).$$

The coefficients a_{ij} and b_{ij} are given by

$$a_{ij} = \sum_k \int_{E_i}^{E_i/\alpha_k^*} f_k(E_i, E') B_j(E') dE' \tag{4.23}$$

and

$$b_{ij} = \sum_k \int_{E_i/\alpha_k^*}^{E_i/\alpha_k} f_k(E_i, E') B_j(E') dE'. \tag{4.24}$$

The quantities $B_j(E')$, a_{ij}, and b_{ij} equal zero when $j < i$. When $j = i$,

$$a_{ii} = \begin{cases} \sum_k \int_{E_i}^{E_i/\alpha_k^*} f_k(E_i, E') B_i(E') dE' & \text{for } E_i/\alpha_k^* \le E_{i+1}, \\ \sum_k \int_{E_i}^{E_{i+1}} f_k(E_i, E') B_i(E') dE' & \text{for } E_i/\alpha_k^* > E_{i+1}. \end{cases} \tag{4.25}$$

For $0 < m < N$,

$$a_{i,i+m} = \begin{cases} 0 & \text{for } E_i/\alpha_k^* \le E_{i+m-1}, \\ \sum_k \int_{E_{i+m-1}}^{E_i/\alpha_m^*} f_k(E_i, E') B_{i+m}(E') dE' & \text{for } E_i/\alpha_k^* \le E_{i+m+1}, \\ \sum_k \int_{E_{i+m-1}}^{E_{i+m+1}} f_k(E_i, E') B_{i+m}(E') dE' & \text{for } E_i/\alpha_k^* > E_{i+m+1}. \end{cases} \tag{4.26}$$

When $j = N$, the last term in the sum is

$$a_{i,N} = \begin{cases} 0 & \text{for } E_i/\alpha_k^* \le E_{N-1}, \\ \sum_k \int_{E_{N-1}}^{E_i/\alpha_k^*} f_k(E_i, E') B_N(E') dE' & \text{for } E_i/\alpha_k^* \le E_N, \\ \sum_k \int_{E_{N-1}}^{E_N} f_k(E_i, E') B_N(E') dE' & \text{for } E_i/\alpha_k^* > E_N. \end{cases} \tag{4.27}$$

The integral in equation (4.24) can be written as

$$\int_{E_i/\alpha_m^*}^{E_i/\alpha_m} f_m(E_i,E')B_j(E')dE' \tag{4.28}$$

$$= \int_{E_i}^{E_i/\alpha_m} f_m(E_i,E')B_j(E')dE' - \int_{E_i}^{E_i/\alpha_m^*} f_m(E_i,E')B_j(E')dE',$$

and is computed in a manner similar to the a_{ij} terms.

Let $\Delta x = L/M$ be the step size used to numerically solve the neutron transport equation, where M is a positive integer. Divide the interval $0 \le x \le L$ up into discrete values $x_k = k\Delta x$, where $k = 0, 1, 2, \ldots, M$. Define the discrete forward and backward fluence values

$$U_{i,k} = U_i(k\Delta x)$$

and (4.29)

$$V_{i,k} = V_i(k\Delta x),$$

respectively, which are illustrated in Figure 13.

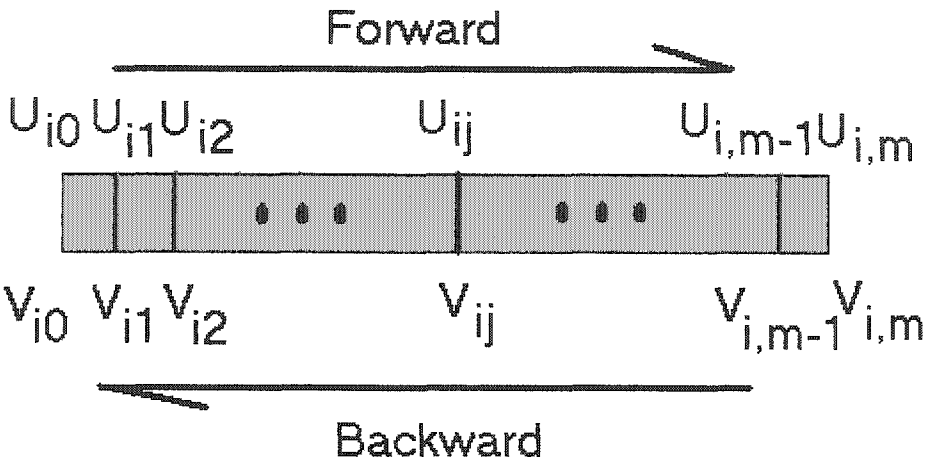

Fig. 13. Forward and backward fluence values for a material slab.

Use the forward and backward difference relations

$$\frac{dU_i}{dx} \approx \frac{U_{i,k+1} - U_{i,k}}{\Delta x} \tag{4.30}$$

and

$$\frac{dV_i}{dx} \approx \frac{V_{i,k} - V_{i,k-1}}{\Delta x}, \tag{4.31}$$

respectively, to approximate derivatives in equations (4.22).

This approximation gives the equations

$$U_{i,k+1} = U_{i,k} + F_{i,k}\Delta x \quad \text{for k} = 0, 1, 2, \ldots, M\text{-}1$$

and (4.32)

$$V_{i,k-1} = V_{i,k} + G_{i,k}\Delta x \quad \text{for k} = M, M\text{-}1, M\text{-}2, \ldots, 1.$$

The index $i = 0, 1, 2, \ldots, N$ in equations (4.32). The boundary conditions are satisfied by setting $U_{i,0} = 0$ and $V_{i,M} = 0$ at the left and right boundaries, respectively. The coefficients $F_{i,k}$ and $G_{i,k}$ are given by

$$\begin{aligned} F_{i,k} &= [a_{i,i} - \sigma(E_i)]U_{i,k} + a_{i,i+1}U_{i+1,k} + \ldots + a_{i,N}U_{N,k} \\ &+ b_{i,i}V_{i,k} + b_{i,i+1}V_{i+1,k} + \ldots + b_{i,N}V_{N,k} + Q_F(x_k, E_i) \end{aligned} \tag{4.33}$$

and

$$\begin{aligned} G_{i,k} &= b_{i,i}U_{i,k} + b_{i,i+1}U_{i+1,k} + \ldots + b_{i,N}U_{N,k} \\ &+ [a_{i,i} - \sigma(E_i)]V_{i,k} + a_{i,i+1}V_{i+1,k} + \ldots + a_{i,N}V_{N,k} + Q_B(x_k, E_i). \end{aligned} \tag{4.34}$$

Equations (4.32) can be solved as a large $2M(N+1)$ square system of linear equations. Writing the system of equations (4.32) in terms of a single index in the form of block matrices gives

$$\begin{bmatrix} A11 & A12 \\ A21 & A22 \end{bmatrix} \begin{bmatrix} X1 \\ X2 \end{bmatrix} = \Delta x \begin{bmatrix} B1 \\ B2 \end{bmatrix}. \tag{4.35}$$

In equation (4.35), $X1$ represents the $M(N+1)$ column vector

$$X1 = col(U_{0,1}, \ldots, U_{0,M}, U_{1,1}, \ldots, U_{1,M}, \ldots, U_{N,1}, \ldots, U_{N,M}), \tag{4.36}$$

$X2$ represents the $M(N+1)$ column vector

$$X2 = col(V_{0,0}, \ldots, V_{0,M-1}, V_{1,0}, \ldots, V_{1,M-1}, \ldots, V_{N,0}, \ldots, V_{N,M-1}), \tag{4.37}$$

$B1$ represents the $M(N+1)$ column vector

$$B1 = col(\, Q_F(x_0, E_0), \ldots, Q_F(x_{M-1}, E_0), \ldots, Q_F(x_0, E_N), \ldots, Q_F(x_{M-1}, E_N)), \quad (4.38)$$

and $B2$ represents the $M(N+1)$ column vector

$$B2 = col(\, Q_B(x_1, E_0), \ldots, Q_B(x_M, E_0), \ldots, Q_B(x_1, E_N), \ldots, Q_B(x_M, E_N)). \quad (4.39)$$

The matrix on the left hand side of equation (4.35) contains the block matrices $A11$, $A12$, $A21$, and $A22$. The block matrices have sub blocks of diagonal elements containing a_{ij} and b_{ij} terms. The forward-backward model uses Gaussian integration to numerically evaluate integrals contained in the a_{ij} and b_{ij} terms. A Gauss-Legendre quadrature formula performs five points per subinterval numerical integration.

Expanding the first equation in (4.32) gives

$$\begin{aligned} U_{i,k+1} = U_{i,k} + \{[a_{i,i} - \sigma(E_i)]U_{i,k} + a_{i,i+1}U_{i+1,k} + \ldots + a_{i,N}U_{N,k}\}\Delta x \\ + \{b_{i,i}V_{i,k} + b_{i,i+1}V_{i+1,k} + \ldots + b_{i,N}V_{N,k} + Q_F(x_k, E_i)\}\Delta x, \end{aligned} \quad (4.40)$$

where $k = 0, 1, 2, \ldots, M-1$.

Expanding the second equation in (4.32) gives

$$\begin{aligned} V_{i,k-1} = V_{i,k} + \{b_{i,i}U_{i,k} + b_{i,i+1}U_{i+1,k} + \ldots + b_{i,N}U_{N,k}\}\Delta x \\ + \{[a_{i,i} - \sigma(E_i)]V_{i,k} + a_{i,i+1}V_{i+1,k} + \ldots + a_{i,N}V_{N,k} + Q_B(x_k, E_i)\}\Delta x, \end{aligned} \quad (4.41)$$

where $k = 1, 2, 3, \ldots, M$.

The index $i = 0, 1, 2, 3, \ldots, N$ in equations (4.40) and (4.41). The index k characterizes depth in the material slab, and index i characterizes neutron energy at depth k. These equations are written as the system of linear equations

$$AX = B. \tag{4.42}$$

To define column vector X in terms of $U_{i,j}$ and $V_{i,j}$, set

$$U_{i,j} = X_{iM+j}, \tag{4.43}$$

where $1 \le iM + j \le M(N+1)$. Let $i = 0, 1, \ldots, N$ and $j = 1, 2, \ldots, M$ in equation (4.43). Set

$$V_{i,j} = X_{M(N+1)+iM+j+1}, \tag{4.44}$$

where $M(N+1)+1 \le M(N+1)+iM+j+1 \le 2M(N+1)$. Let $i = 0, 1, \ldots, N$ and $j = 0, 1, \ldots, M$ - 1 in equation (4.44). The system of equations (4.32) can be written in terms of vector X. At endpoint $k = 0$, the first equation in (4.32) takes the form

$$\begin{aligned} X_{iM+1} = \{&b_{i,i} X_{M(N+1)+iM+1} + b_{i,i+1} X_{M(N+1)+(i+1)M+1} \\ &+ \ldots + b_{i,N} X_{M(N+1)+NM+1} + Q_F(x_0, E_i)\}\Delta x. \end{aligned} \tag{4.45}$$

For $1 \le k \le M - 1$, the first equation in (4.32) takes the form

$$X_{iM+k+1} = X_{iM+k} + \{[a_{i,i} - \sigma(E_i)]X_{iM+k} + a_{i,i+1}X_{(i+1)M+k} + \ldots + a_{i,N}X_{NM+k}\}\Delta x$$

$$+ \{b_{i,i}X_{M(N+1)+iM+k+1} + b_{i,i+1}X_{M(N+1)+(i+1)M+k+1} + \ldots + b_{i,N}X_{M(N+1)+NM+k+1} \quad (4.46)$$

$$+ Q_F(x_k, E_i)\}\Delta x.$$

At end point $k = M$, the second equation in (4.32) takes the form

$$X_{M(N+1)+iM+M} = \{b_{i,i}X_{iM+M} + b_{i,i+1}X_{(i+1)M+M} + \ldots + b_{i,N}X_{NM+M} + Q_B(x_M, E_i)\}\Delta x. \quad (4.47)$$

Finally, for $1 \le k \le M-1$, the second equation in (4.32) takes the form

$$X_{M(N+1)+iM+k} = X_{M(N+1)+iM+k+1} + \{b_{i,i}X_{iM+k} + b_{i,i+1}X_{(i+1)M+k} + \ldots + b_{i,N}X_{NM+k}\}\Delta x$$

$$+ \{[a_{i,i} - \sigma(E_i)]X_{M(N+1)+iM+k+1} + a_{i,i+1}X_{M(N+1)+(i+1)M+k+1} + \ldots \quad (4.48)$$

$$+ a_{i,N}X_{M(N+1)+NM+k+1} + Q_B(x_k, E_i)\}\Delta x.$$

Matrix A is sparse with a nonsymmetrical form. Let $M = 100$ (100 spatial steps) and $N = 62$ (63 energy steps) to have the same number of spatial and energy steps as in the HZETRN code for forward scattered neutrons. Doing this assists in adding the forward-backward model low-energy isotropic neutrons to the HZETRN code high-energy forward scattered neutrons to get the neutron fluence at all energies at the desired depths. Using these values for M and N produces a system of 12,600 equations in 12,600 unknowns. Multiplying $M(N+1)$ by 2, for the forward and backward directions, gives 12,600. Do a LU decomposition of matrix A and solve for the unknowns using back substitution. The forward-backward model code numerically solved the above system of equations using NETLIB LU decomposition FORTRAN 77 routines SGECO.F and

SGESL.F. The time needed for a 500 MHz DEC alpha machine to reach a solution for a single slab of material was approximately 30 minutes. Numerical solutions involve truncation error, stability, and convergence issues. Truncation error is investigated in Appendix B, and Appendix C gives a discussion of stability and convergence.

The Shield and Target Configuration

The procedures used to solve the neutron Boltzmann equation for a shield and target configuration are similar to those used for a single slab. The shield and target configuration uses an iterative process to satisfy continuity conditions to within a specified tolerance at the boundary interface. The shield and target materials have lengths L and L', respectively. The lengths L and L' may equal each other. Figure 14 illustrates the shield and target configuration including the discretized forward and backward fluence components. The shield and target materials are each divided up into m spatial steps with index i depicting neutron energy. The spatial step sizes used in the forward-backward model were $\Delta x = L/m$ and $\Delta x' = L'/m$ for the shield and target materials, respectively. If the shield and target materials have equal lengths then the step sizes are equal. The forward-backward model code allows for either equal or unequal step sizes to be used.

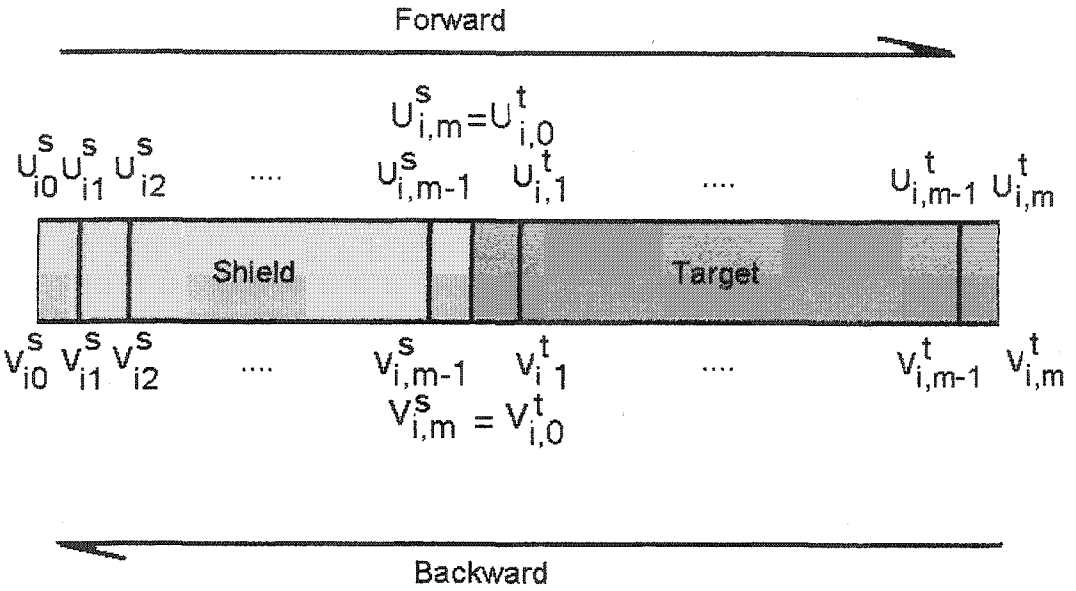

Fig. 14. Shield and target configuration.

Continuity of forward and backward fluence at the shield and target interface is required. The continuity conditions at the boundary interface are given by

$$\Phi_F^T(0,E) = \Phi_F^S(L,E) \tag{4.49}$$

and

$$\Phi_B^S(L,E) = \Phi_B^T(0,E). \tag{4.50}$$

In equation (4.49), $\Phi_F^T(0,E)$ represents forward moving fluence at depth 0 in the target material and $\Phi_F^S(L,E)$ represents forward moving fluence at depth L in the shield material. In equation (4.50), $\Phi_B^S(L,E)$ represents backward moving fluence at depth L in

the shield material and $\Phi_B^T(0,E)$ represents backward moving fluence at depth 0 in the target material.

The iteration procedure first solves for neutron fluence in the shield material using the boundary conditions $\Phi_F^S(0,E) = \Phi_B^S(L,E) = 0$. The forward-backward model code is run a second time to determine neutron fluence in the target material. Forward fluences computed at the right edge of the shield material are used as boundary conditions at the left edge of the target material. This is expressed in the equation $\Phi_F^T(0,E) = \Phi_F^S(L,E)$ and establishes continuity of forward fluence at the shield and target interface. Use the boundary condition $\Phi_B^T(L',E) = 0$ at the right edge of the target material. Backward fluence solutions at the left edge of the target material are compared to backward fluence solutions at the right edge of the shield material from the previous run. If backward fluence solutions at the boundary interface from two successive runs are within a specified tolerance of each other for all energies, then continuity in backward fluence at the interface is achieved. Solution to the neutron transport equation for the shield and target configuration is reached when the boundary and continuity conditions are satisfied. No solution is found if the backward fluence at the target material's left boundary is not within a given tolerance of the backward fluence at the shield material's right boundary for all energies. If no solution was found, the code must be run again for the shield material using backward fluences computed at the left edge of the target material as the new boundary condition for backward fluences at the right edge of the shield material. The process of computing neutron fluences in the shield and target materials is repeated until a solution is found, or a maximum number of iterations are performed. If the

maximum number of iterations is reached, then no solution to the neutron Boltzmann equation for the shield and target configuration was determined.

It should be noted that an alternative method was also used to solve the Boltzmann neutron transport equation for the shield and target configuration. This alternative method is very similar to the procedure used to solve for neutron fluence in a single slab of material. The length of material is increased from L to $L + L'$ to represent the combined lengths of shield and target. Parameters used to describe properties of the shield and target materials are adjusted in the forward-backward model code to reflect their dependence on depth. The continuity conditions at the shield and target boundary interface are automatically satisfied.

The alternative method of solving the Boltzmann neutron transport equation uses larger matrices than the first method. Larger matrices increase computer memory requirements and the time needed to reach a solution. For a single material, energy and depth grids were chosen that resulted in solving a system of 12,600 equations in 12,600 unknowns. The first method repeatedly solved this system until a solution to the shield and target configuration was found. The alternative method resulted in solving a system of 25,200 equations in 25,200 unknowns for the same neutron energies and depths used in the first method. The 25,200 by 25,200 matrix was too large for the DEC alpha machine at NASA Langley Research Center; therefore the code was run on the high performance computer at Old Dominion University.

For an aluminum shield followed by a water target configuration, the CPU time needed to reach a solution using the alternative method was over 44 hours. The first

method required approximately 2 hours to reach a solution. The two methods gave similar neutron fluence results. The computer memory needed to accommodate smaller matrices using the first method is substantially less than that needed for larger matrices using the alternative method. Therefore, the first method of solving the Boltzmann neutron transport equation for a shield and target configuration is preferred over the alternative method when using the forward-backward model.

CHAPTER V

RESULTS AND CONCLUSIONS

Forward-backward model solutions to the low-energy neutron transport equation are compared to Monte Carlo MCNPX results in the next section. This Monte Carlo code comes from a merger of the Los Alamos High-Energy Transport (LAHET) and Monte Carlo N-Particle (MCNP) transport codes[13]. The forward-backward model and HZETRN codes compute neutron fluences, but at different energies. Linear interpolation of neutron fluence as a function of energy is needed to add results given by the two methods. Adding forward-backward model isotropic evaporation neutrons to HZETRN code forward moving high-energy neutrons gave results that are in good agreement with Monte Carlo solutions. For energies $E < 4$ MeV, forward-backward model isotropic evaporation neutrons added significantly to HZETRN code forward moving high-energy neutrons. The number of neutrons added is comparatively small at energies $E \geq 4$ MeV.

Solutions to the Neutron Transport Equation

Neutron fluences computed by the Monte Carlo code MCNPX are used for comparison purposes in the figures that follow. If an infinite number of particle histories are performed using an unbiased Monte Carlo method, then the correct solution will result. Time limitations allow for only a finite number of histories, and statistical methods are utilized to quantify the results. The MCNPX code allows continuous energy and multigroup cross section input. Continuous energy best models the physics of neutron transport, but multigroup methodology is computationally faster. Monte Carlo

result accuracy depends on the statistical methodology, geometrical representations, and accuracy of physical models used in the problem. MCNPX results were generated by modeling a set of proton beams incident on a slab of material. The proton beams, and secondary particles produced, were integrated using a probability distribution to mimic the February 23, 1956 solar proton event. Information regarding neutron transport and diffusion in the MCNPX and NASA HZETRN codes, respectively, are given in references [19] and [20], respectively.

The HZETRN code was used to generate isotropic neutron source terms produced in a slab of material exposed to the largest recorded solar particle event of February 23, 1956. The February 1956 event was chosen because it involved the production of large numbers of protons. Numerous evaporation and cascading neutrons are produced when protons bombard shield materials. The February 23, 1956 solar particle event models a worst-case scenario of radiation environment that astronauts could be exposed to on a mission. High-energy cascading neutrons with energies $E > 100$ MeV produce low-energy evaporation neutrons having energies $E < 100$ MeV. Low-energy evaporation neutrons computed by the HZETRN code are neutron source terms used in the forward-backward model.

Figure 15 illustrates the neutron fluence at a depth of $50\ \mathrm{g/cm^2}$ in an $100\ \mathrm{g/cm^2}$ aluminum slab exposed to the February 23, 1956 solar particle event. The HZETRN and Monte Carlo method solutions are compared. The HZETRN results shown in this figure were obtained using a multigroup solution for isotropic low-energy neutrons. The labels Total, Forward, and Backward specify fluence directions. The HZETRN neutron fluence

is less than the Monte Carlo results at energies $E < 4$ MeV, and methods giving more accurate solutions at these energies are needed. The forward-backward model is a deterministic code for obtaining accurate neutron fluences at energies $E < 4$ MeV. The HZETRN and Monte Carlo method neutron fluences are in good agreement for energies $E \geq 4$ MeV.

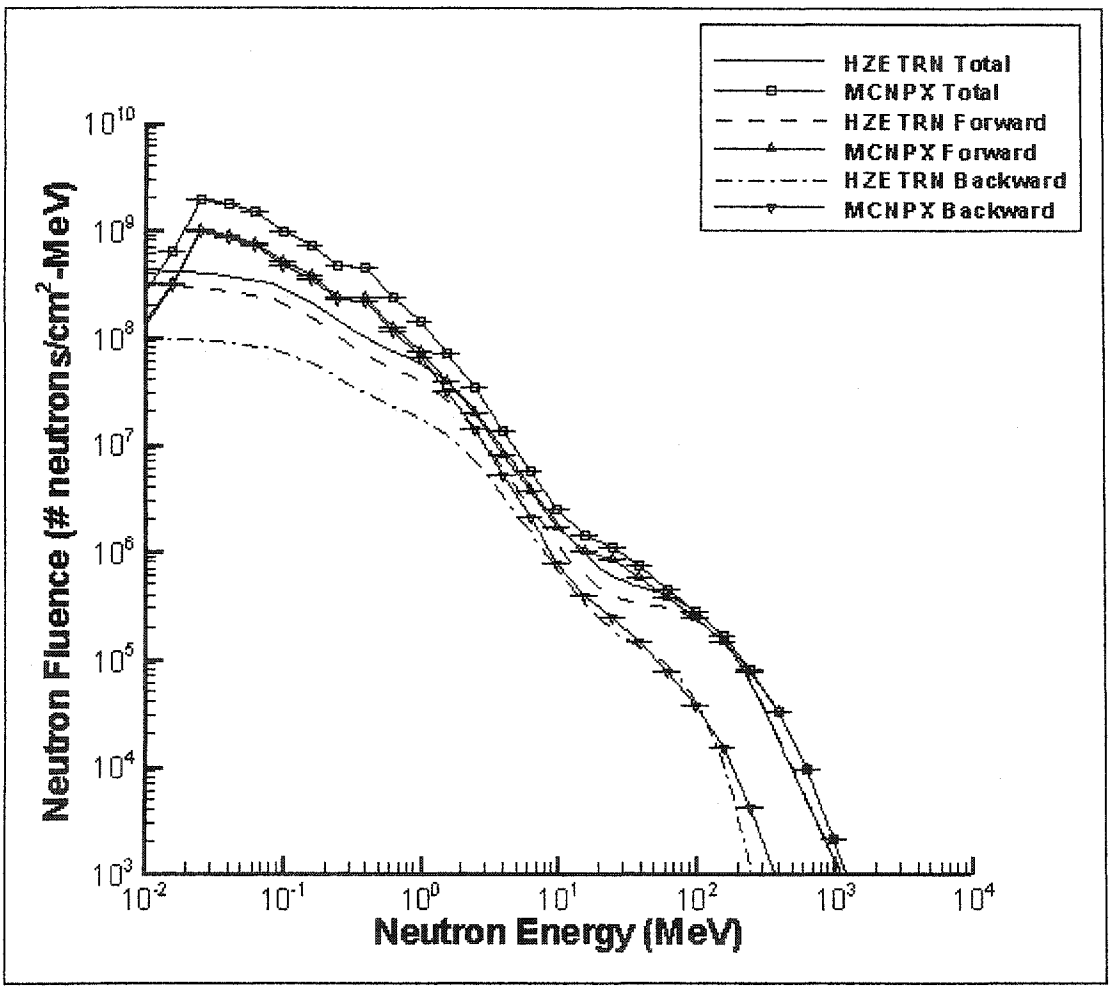

Fig. 15. Neutron fluence at 50 g/cm^2 in an 100 g/cm^2 aluminum slab exposed to the February 23, 1956 solar particle event.

In the following figures, FBM indicates forward-backward model results. Figure 16 illustrates the neutron fluence at depth $50\,g/cm^2$ in an $100\,g/cm^2$ aluminum slab exposed to the February 23, 1956 solar particle event. Monte Carlo and forward-backward model solutions are illustrated. The forward-backward model forward neutron fluence illustrated in the figure is the sum of the forward-backward model and HZETRN code forward moving neutrons. The HZETRN code used a perturbation method to calculate the transport of forward moving high-energy neutrons. Fluences obtained using the forward-backward model and Monte Carlo codes are in good agreement in the high-energy range, $E > 100$ MeV.

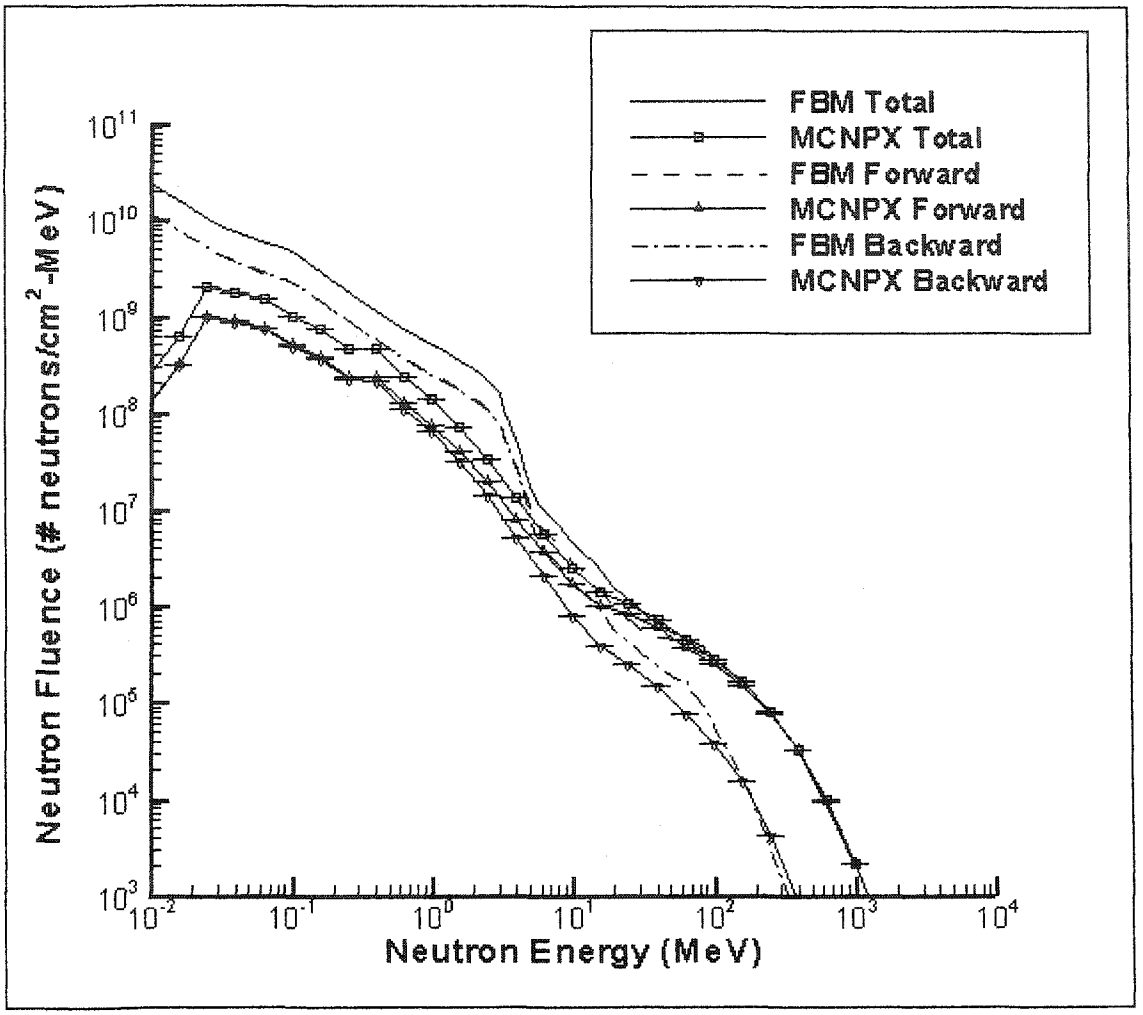

Fig. 16. Neutron fluence at 50 g/cm^2 in an 100 g/cm^2 aluminum slab exposed to the February 23, 1956 solar particle event.

Figure 17 is a plot of the neutron fluence at 20 g/cm^2 in an 100 g/cm^2 copper slab exposed to the February 23, 1956 solar particle event. HZETRN forward moving high-energy neutrons were not added to the forward-backward model forward neutron fluence. The forward-backward model solutions are less than the Monte Carlo results at energies $E > 100$ MeV. Adding the HZETRN and forward-backward model forward moving neutrons together corrects this error.

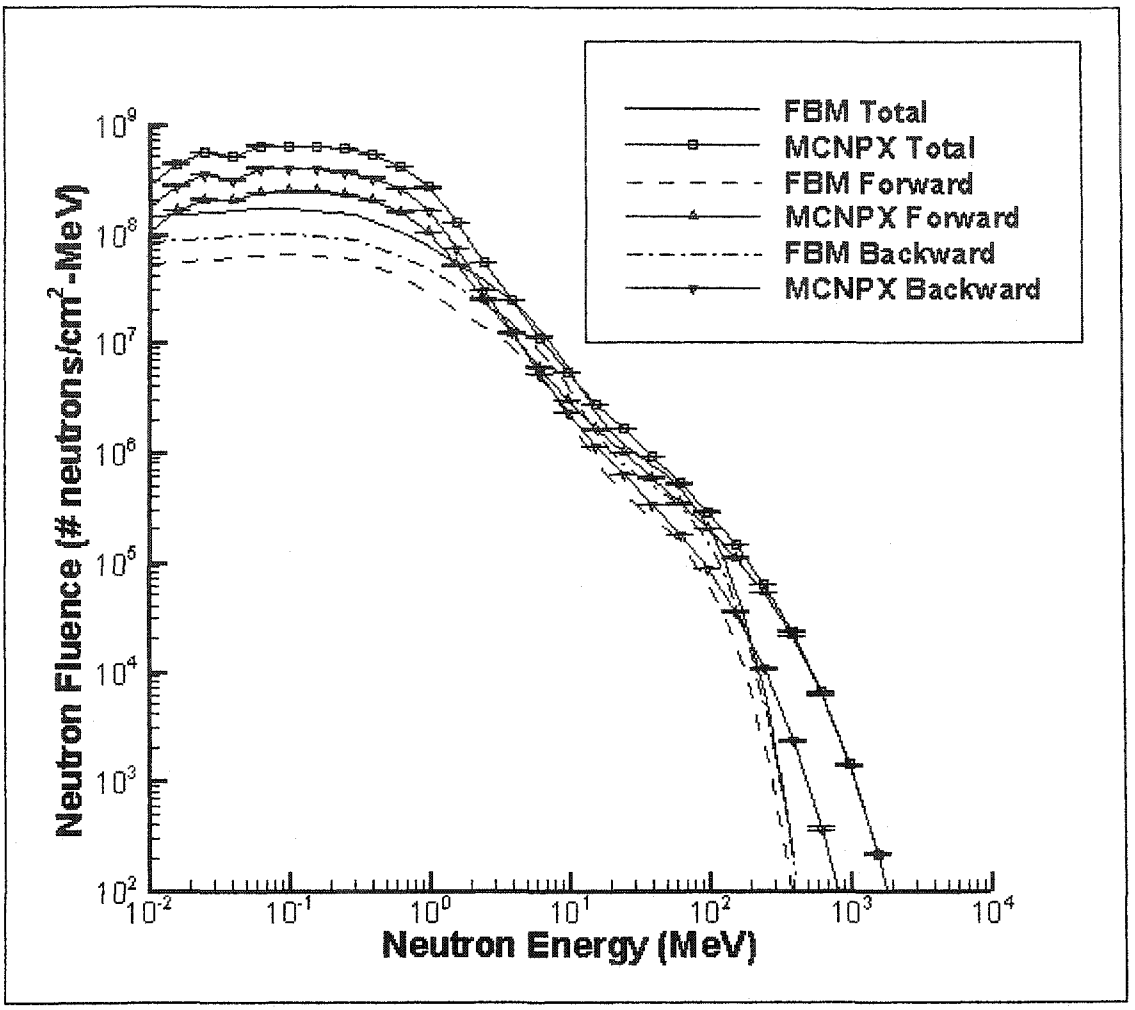

Fig. 17. Neutron fluence at 20 g/cm^2 in an 100 g/cm^2 copper slab exposed to the February 23, 1956 solar particle event.

The surface material of Mars is called Martian regolith, and is composed mainly of oxygen (O), magnesium (Mg), silicon (Si), calcium (Ca), and iron (Fe). These elements are combined together to form the compounds SiO_2, FeO_3, MgO, and CaO. Martian regolith is 58.2% SiO_2, 23.7% FeO_3, 10.8% MgO, and 7.3% CaO. Information regarding the composition of Martian regolith was taken from reference [13]. Figure 18 illustrates forward-backward model and Monte Carlo method neutron fluences

at 50 g/cm^2 in an 100 g/cm^2 Martian regolith slab exposed to the February 23, 1956 solar particle event. HZETRN forward moving high-energy neutrons were added to the forward-backward model results.

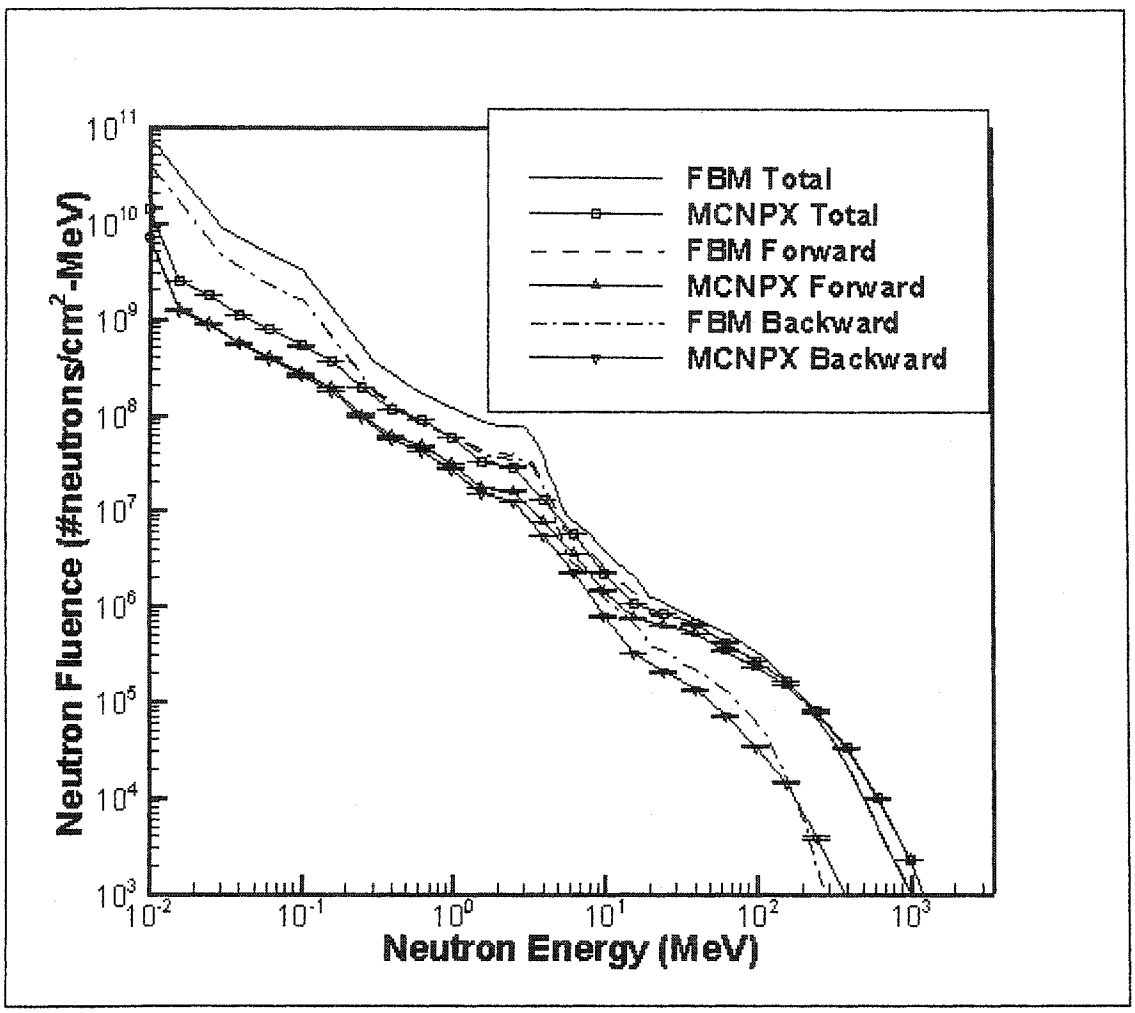

Fig. 18. Neutron fluence at 50 g/cm^2 in an 100 g/cm^2 Martian regolith slab exposed to the February 23, 1956 solar particle event.

Radiation protection research scientists at NASA determine the amount and type of shielding materials used to protect astronauts from harmful space radiation. The

International Space Station and space shuttle are constructed mainly of aluminum, which acts as a shielding material for astronauts located inside these structures. Water is used as a target material to represent astronauts in computer models because it is the primary component in human beings. Therefore, it is of interest to determine the neutron fluence at various depths and energies in an aluminum shield followed by a water target configuration.

Figure 19 illustrates that neutron fluence changes with depth for particular neutron energies in a shield followed by a target configuration. The shield and target are $100\,g/cm^2$ slabs of aluminum and water, respectively. The neutron fluences were obtained using the forward-backward model. As neutron energy increases, the neutron fluence diminishes in the shield and target materials. Neutron production cross sections tend to decrease with increasing energy. The lowering trend in neutron fluence versus depth continues for increasing neutron energy, and roughly converges to a constant fluence at all depths in the shield and target materials. It can be seen from the figure that neutron fluence does not change abruptly at the shield and target interface. This can be attributed to neutrons leaving the aluminum shield and traveling a short distance into the water target before being absorbed. The apparent point where shield and target fluences meet is slightly shifted to the right of the boundary interface.

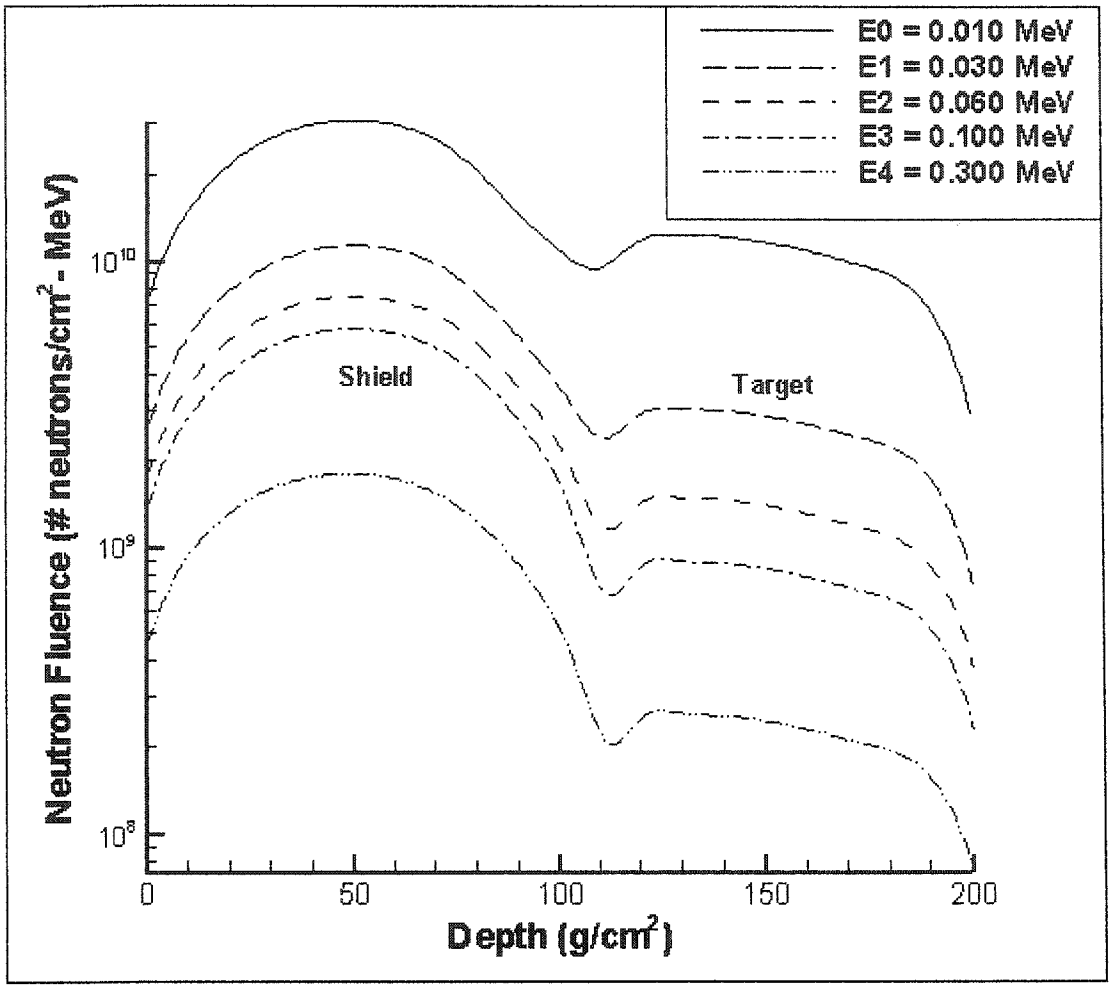

Fig. 19. Neutron fluence versus depth in 100 g/cm^2 of aluminum shield followed by 100 g/cm^2 of water target.

Figure 20 is a plot of neutron fluence versus energy at 50 g/cm^2 in 100 g/cm^2 of aluminum shield followed by 100 g/cm^2 of water target. The forward-backward model and Monte Carlo method results are in good agreement. Neutron fluence roughly exhibits a $1/E$ behavior on a log-log scale for energies $E \leq 100$ MeV. The HZETRN code forward moving neutrons are incorporated into the forward-backward model results that are illustrated in Figures 20 through 25.

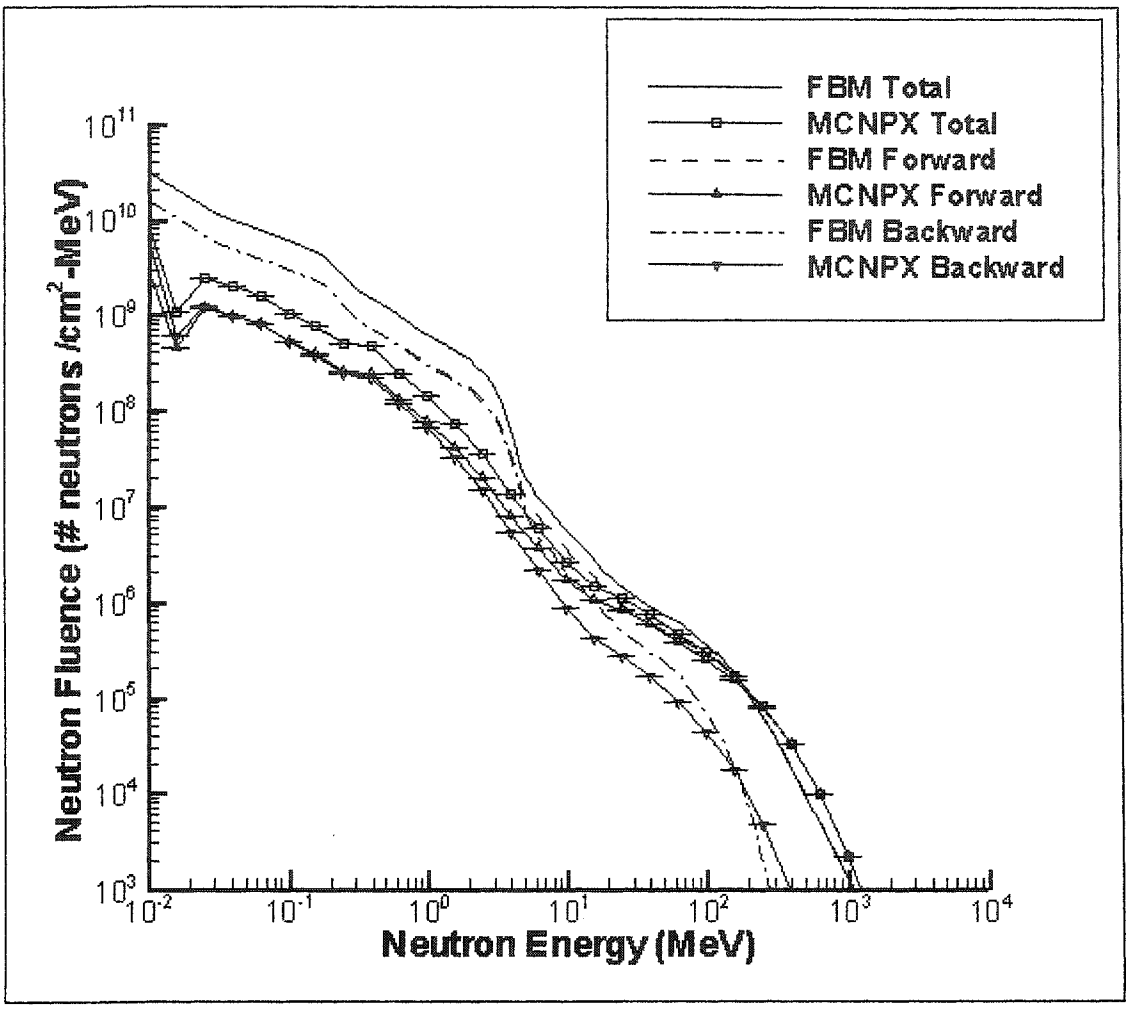

Fig. 20. Neutron fluence at 50 g/cm^2 in 100 g/cm^2 of aluminum shield followed by 100 g/cm^2 of water target.

Figure 21 is a plot of neutron fluence versus energy at 100 g/cm^2 in 100 g/cm^2 of aluminum shield followed by 100 g/cm^2 of water target. This depth is at the boundary interface separating the two materials. The forward-backward model and Monte Carlo method neutron fluences are in good agreement.

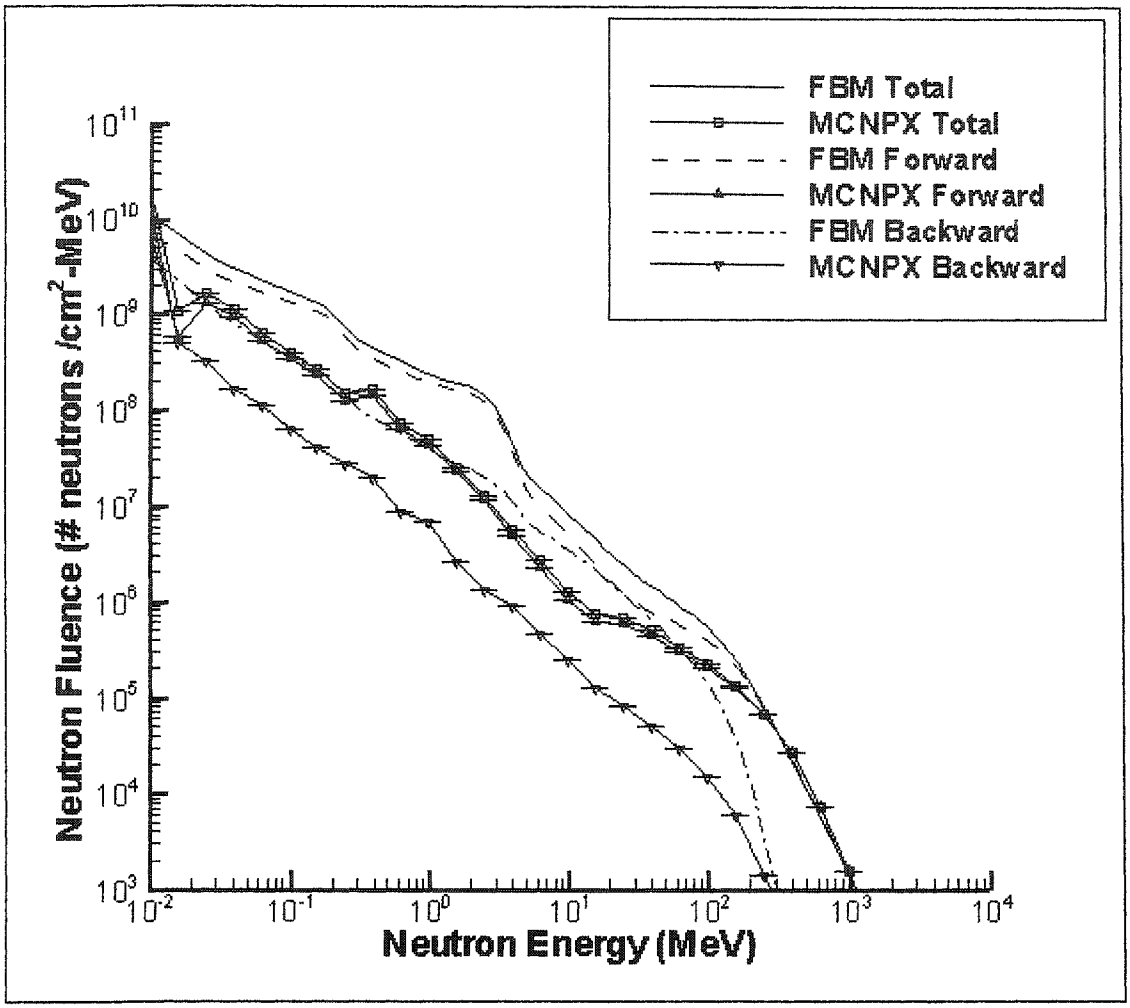

Fig. 21. Neutron fluence at 100 g/cm^2 in 100 g/cm^2 of aluminum shield followed by 100 g/cm^2 of water target.

Figure 22 illustrates neutron fluence at 150 g/cm^2 in the aluminum shield and water target configuration. This depth is one half the total distance into the water target. The forward-backward model and Monte Carlo results are no longer in good agreement at energies $E < 400$ MeV. This may be due to discrepancies in the cross sections used in the forward-backward model over this energy range. Scattering cross sections were functions of depth and incident neutron energy, not scattering angle. Omitting the

scattering angle dependence is a source of error in computed neutron fluence. Researchers at NASA Langley Research Center are currently improving the cross sections used in numerical simulations of particle transport in shielding materials. Materials rich in light ions, such as hydrogen, are hardest to model in a one-dimensional geometry due to elastic scattering in all directions. Another possible source of error is in the set up and execution of Monte Carlo code MCNPX. The MCNPX plots displayed in this manuscript differ from those presented in reference [20] at corresponding depths in the aluminum shield followed by a water target configuration. The forward-backward model results agree more closely with the MCNPX plots shown in reference [20]. Monte Carlo codes should be run several times and the results averaged to get an accurate solution. To do this requires a great deal of computer resources and time. Radiation research scientists at NASA Langley Research Center are planning on running the MCNPX code in the near future to generate accurate Monte Carlo results.

In the MCNPX results there is a large increase in neutron fluence at energy $E = 10^{-2}$ MeV. This increase results from adding together all of the neutrons having energies $E \leq 10^{-2}$ MeV and plotting them in the $E = 10^{-2}$ MeV energy bin. Transport codes model the physics of all the different types of particle interactions that occur in a slab of material exposed to a radiation field. The Monte Carlo code MCNPX is a transport code. Diffusion codes describe particles that scatter off of each other and move from regions of higher to lower concentrations. The forward-backward model has both transport and diffusion code characteristics incorporated in its cross sections. Neutrons in a highly scattering media, such as water, migrate more quickly from higher to lower

energies when modeled using a transport code. In a low scattering material, such as aluminum, neutrons maintain their higher energies when modeled using a transport code. The diffusion code characteristic of the forward-backward model leads to an over prediction of neutron fluence in water.

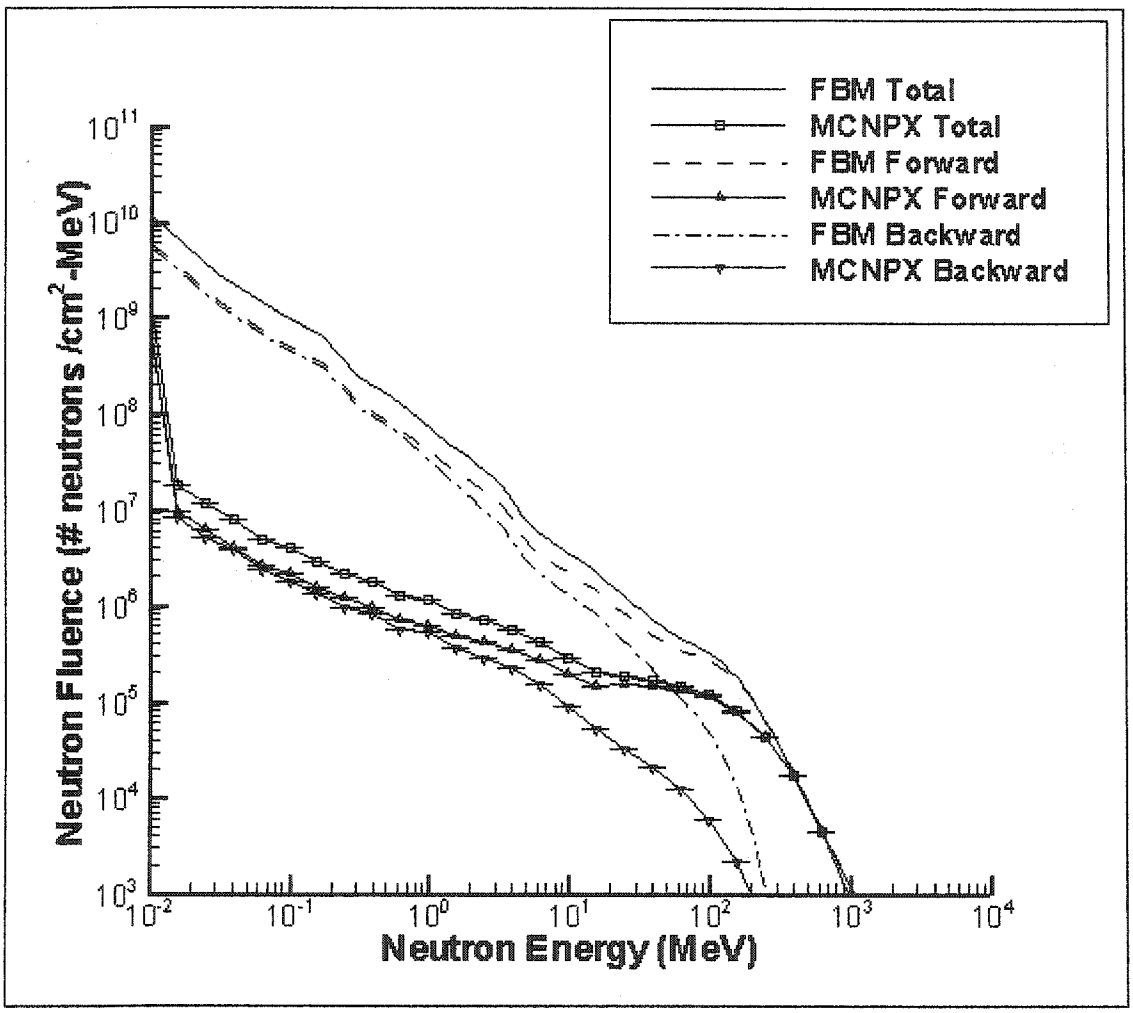

Fig. 22. Neutron fluence at 150 g/cm^2 in 100 g/cm^2 of aluminum shield followed by 100 g/cm^2 of water target.

Figures 23 through 25 illustrate forward-backward model and MCNPX neutron fluence versus energy curves at other depths in the aluminum shield followed by a water

target configuration. There is good agreement between results from the two methods in the aluminum shield. The forward-backward model exceeds MCNPX results at energies $E < 400\,\text{MeV}$ in the water target.

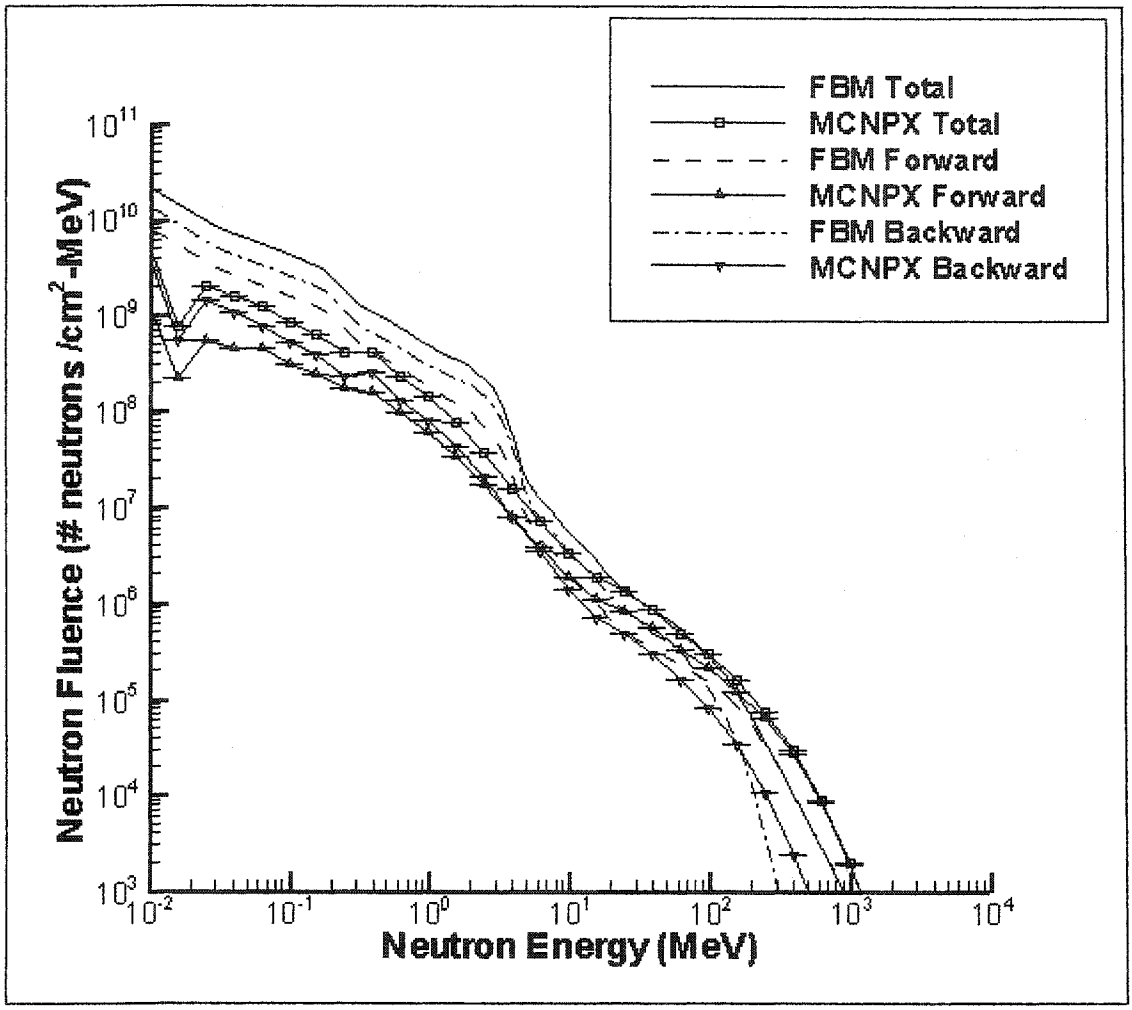

Fig. 23. Neutron fluence at $20\,\text{g/cm}^2$ in $100\,\text{g/cm}^2$ of aluminum shield followed by $100\,\text{g/cm}^2$ of water target.

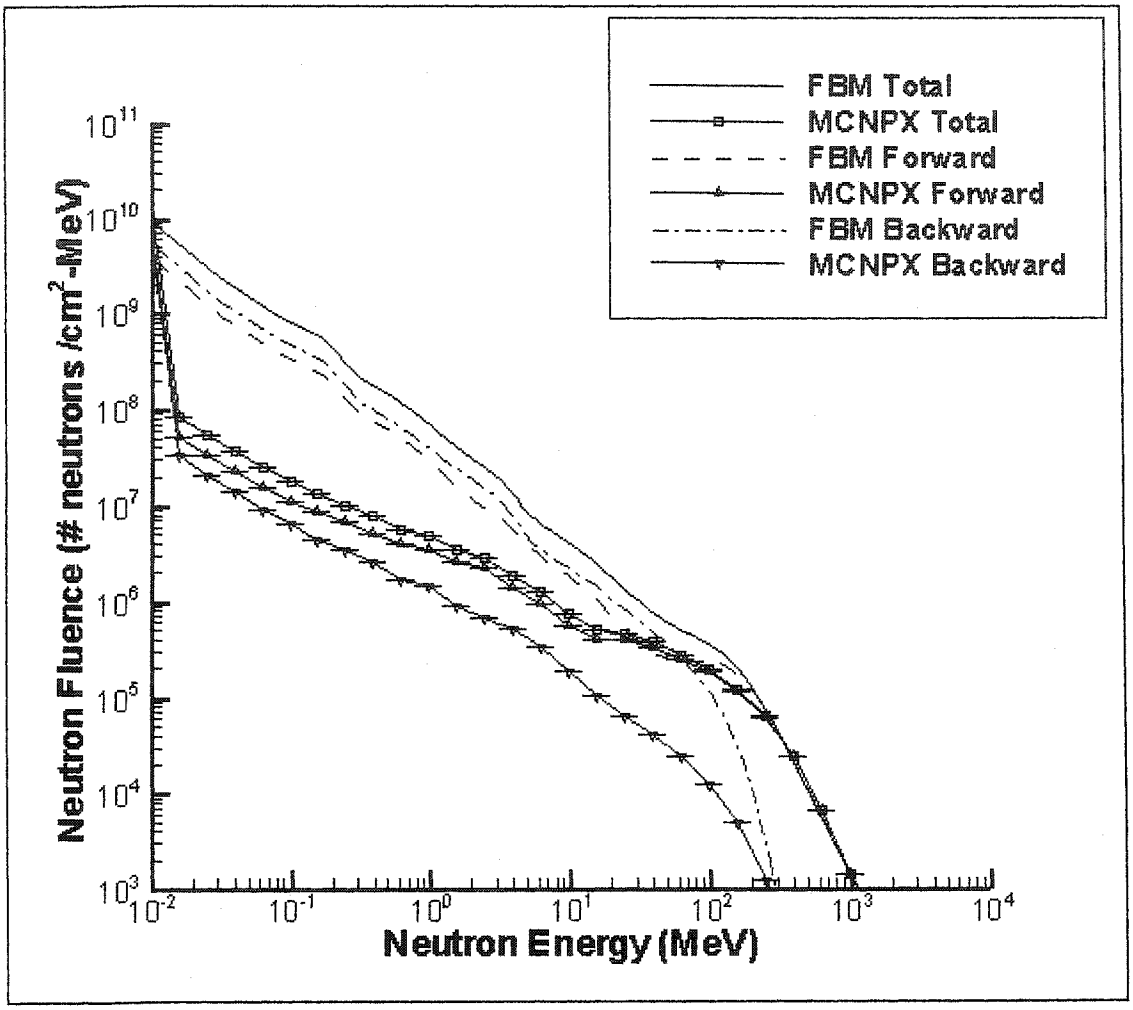

Fig. 24. Neutron fluence at 110 g/cm^2 in 100 g/cm^2 of aluminum shield followed by 100 g/cm^2 of water target.

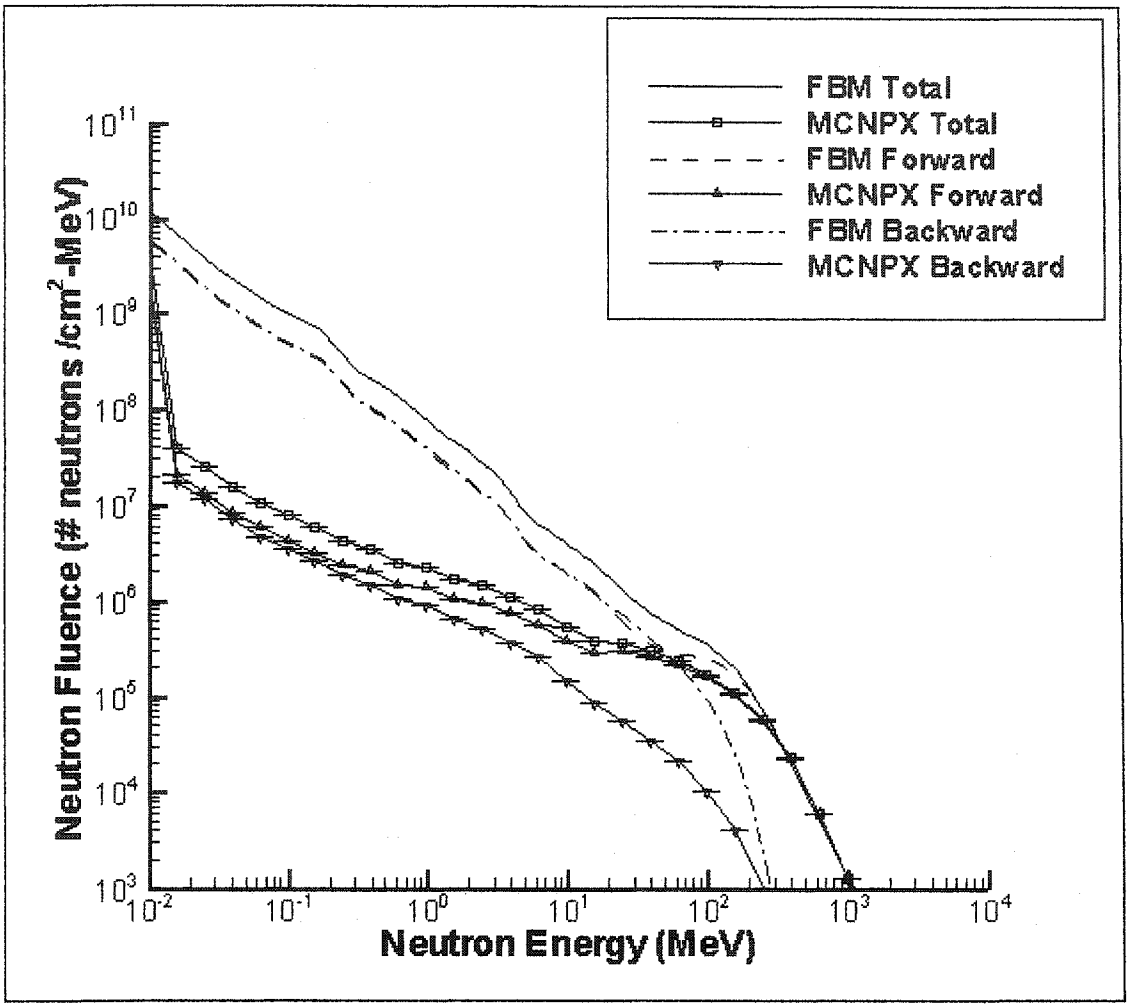

Fig. 25. Neutron fluence at 120 g/cm^2 in 100 g/cm^2 of aluminum shield followed by 100 g/cm^2 of water target.

Experimentally determined neutron total and elastic scattering cross sections were substituted for forward-backward model computed cross sections to determine if more accurate solutions in the shield and target configuration would result. The experimentally determined cross sections were taken from databases maintained by Los Alamos and Oak Ridge National laboratories[21]. Neutron fluences calculated using cross sections taken from databases were similar to computed cross section fluences. The computed and database cross sections did not include dependence on scattering angle.

Figure 26 illustrates low-energy neutron fluences that were computed using various methods at $50\,g/cm^2$ in an $100\,g/cm^2$ aluminum slab exposed to the February 23, 1956 solar particle event[22]. The forward-backward model (fb), P_N method (Pn), S_N method (Sn), and Monte Carlo method (mc) were used to calculate these fluences. The Monte Carlo method includes high and low energy neutrons in its results, but the forward-backward model, P_N method, and S_N method results do not. The HZETRN code high-energy neutron fluence is also illustrated in the figure. The forward-backward model fluence compares favorably with the results obtained using the other methods at energies $E \leq 4\,MeV$.

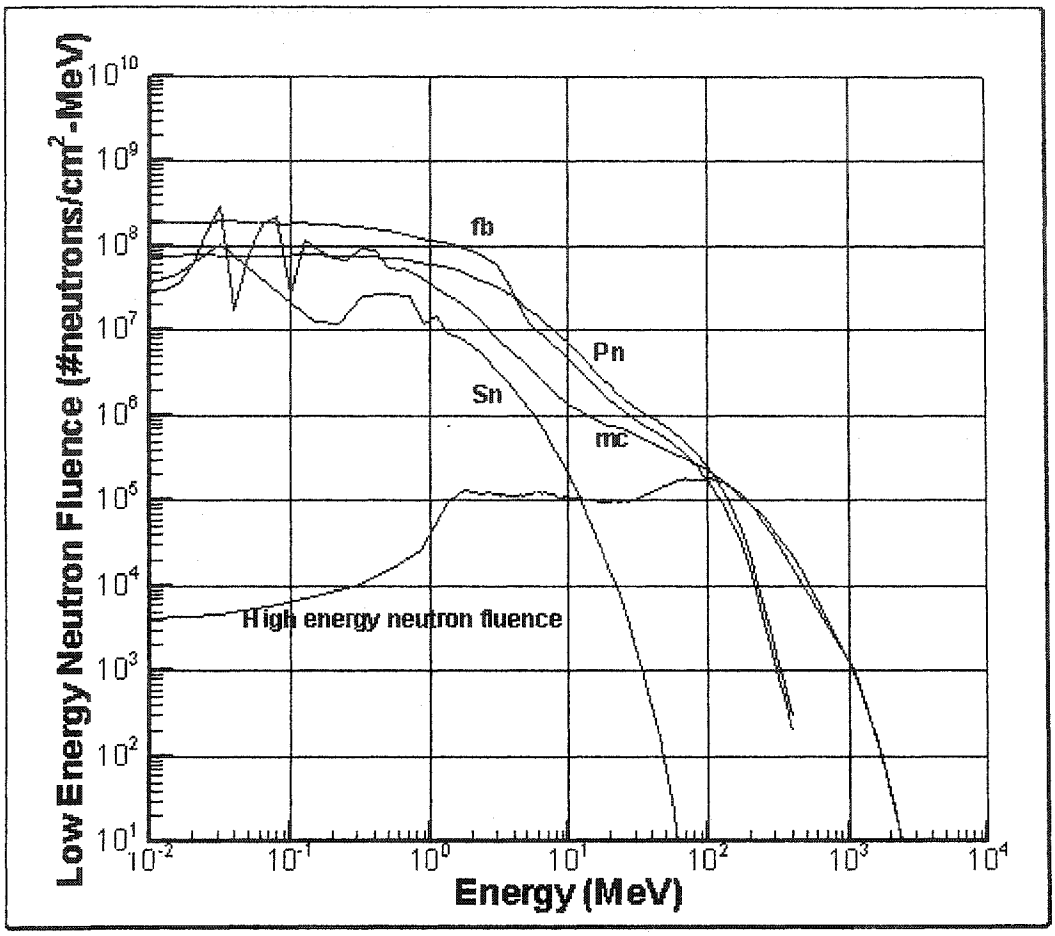

Fig. 26. High and low-energy neutron fluence at $50\,g/cm^2$ in an $100\,g/cm^2$ aluminum slab exposed to the February 23, 1956 solar particle event.

Figure 27 illustrates the total neutron fluence obtained by adding the HZETRN code high-energy neutrons to the low-energy neutrons that were computed using the same methods illustrated in the previous figure[22]. Variations in the curves are attributed to the types of cross sections used in the different methods. The forward-backward model and P_N method used approximate HZETRN code computed cross sections. The Monte Carlo and S_N methods used ANISN cross sections. The ANISN cross sections include resonance energies that produce variations in the computed neutron fluences illustrated in Figure 27. The forward-backward model solutions are in good agreement with the results

obtained using the other methods at all energies. With more accurate neutron scattering cross sections the forward-backward model results are expected to improve.

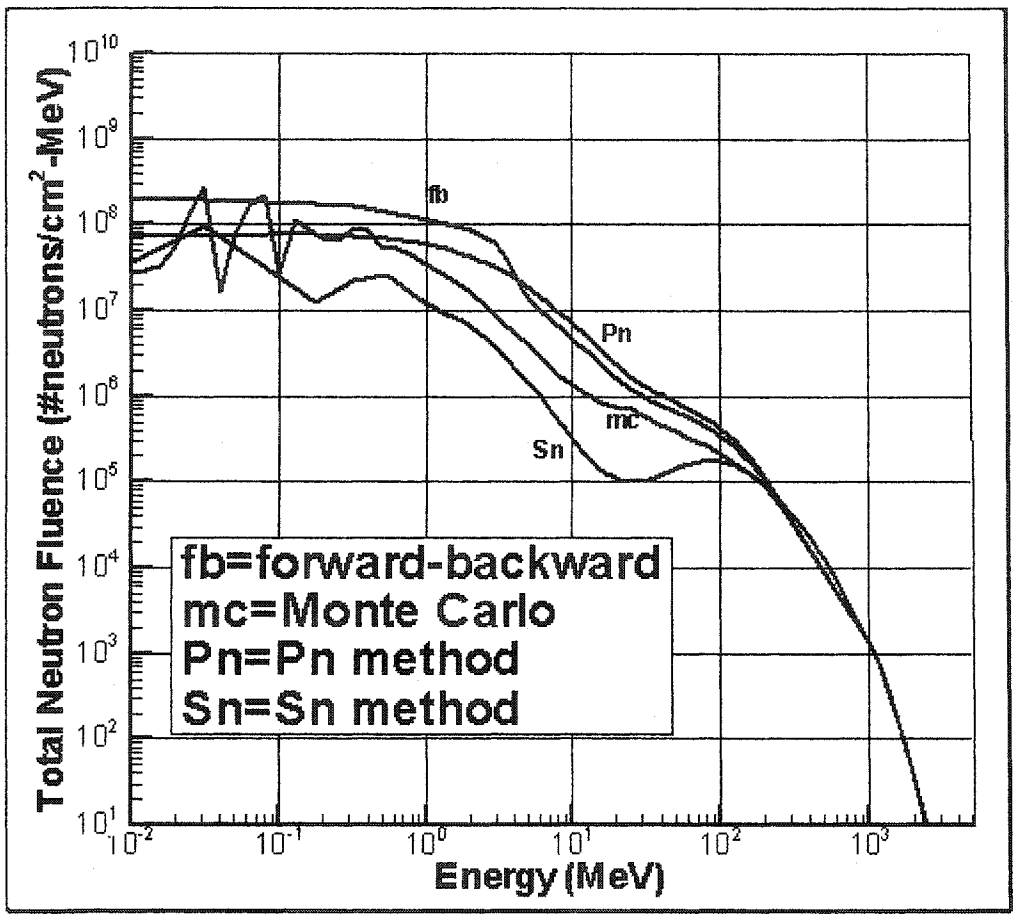

Fig. 27. Total neutron fluence at 50 g/cm^2 in an 100 g/cm^2 aluminum slab exposed to the February 23, 1956 solar particle event.

Summary

The low-energy neutron radiation environment in a material slab was determined by solving a coupled system of integro-differential Boltzmann equations with source terms. The integro-differential equations were transformed into a coupled system of ordinary differential equations by introducing a series of linear B-splines. Substituting

forward and backward difference approximations for spatial derivatives made it possible to reduce the problem to solving a large linear system of equations having the form $Ax = B$. Solution to the large linear system of equations was given in the form of a vector x representing the neutron fluence at M depths and $N+1$ energies. This gave $2M(N+1)$ equations in $2M(N+1)$ unknowns. Letting $M = 100$ and $N = 62$ gave results at depths and energies similar to those used in the HZETRN code. These values for M and N gave a linear system of 12,600 equations in 12,600 unknowns in the form $Ax = B$, and were solved using the Lower Upper (LU) decomposition method and back substitution. In the LU decomposition method the letters L and U represent lower and upper triangular matrices, respectively. Decomposition of matrix A into a product of lower and upper triangular matrices is expressed in the equation $A = LU$. Substituting the matrix product LU for matrix A yields the equation $LUx = B$. Letting vector $y = Ux$ creates a new triangular system of linear equations in the form $Ly = B$ that is easily solved for vector y using back substitution. The triangular system of linear equations $Ux = y$ is solved for the unknown vector x using back substitution a second time. Vector x contains the forward and backward neutron fluence solutions predicted by the Boltzmann neutron transport equation.

The amount of time needed to reach a solution using the forward-backward model for a single shield material was approximately 30 minutes on a DEC alpha 500 MHz machine. The amount of time needed to reach a solution using Monte Carlo methods was over 7 days on a SGI 250 MHz machine. The forward-backward model and Monte Carlo solutions are in good agreement in a single shield material. Approximately 2 hours were needed to solve the forward-backward model system of equations for a shield and target

configuration on a DEC alpha 500 MHz machine. Weeks of calculations were needed using Monte Carlo methods on a SGI 250 MHz machine for the same shield and target configuration. The forward-backward model and Monte Carlo solutions are in good agreement in the shield material for the shield and target configuration.

Conclusions

The forward-backward model is more accurate than the multigroup method in predicting low-energy isotropic neutron fluences in shielding materials. The forward-backward model requires significantly less time than Monte Carlo methods to reach a solution to the low-energy neutron Boltzmann equation. Therefore, the forward-backward model generates in a relatively short period of time accurate low-energy neutron fluences in slabs of material that are bombarded by energetic particles. The forward-backward model may be incorporated into the HZETRN code at NASA Langley Research Center to assist in the quick and accurate computing of radiation environments in space vehicles and habitats.

BIBLIOGRAPHY

1. J. W. WILSON, L. W. TOWNSEND, W. SCHIMMERLING, G. S. KHANDELWAL, F. KHAN, J. E. NEALY, F. A. CUCINOTTA, L. C. SIMONSEN, J. L. SHINN, J. W. NORBURY, *Transport Methods and Interactions for Space Radiations*, NASA RP-1257, National Aeronautics and Space Administration (1991).

2. K. S. KRANE, *Introductory Nuclear Physics*, John Wiley & Sons, Inc. (1988).

3. R. BERTELL, http://www.ratical.org/radiation/NRBE/NRadBioEffects.html, *No Immediate Danger, Prognosis for a Radioactive Earth*, The Book Publishing Company (2003).

4. National Council on Radiation Protection and Measurements Report #92, *Public Radiation Exposure from Nuclear Power Generation in the United Sates* (1987).

5. National Council on Radiation Protection and Measurements Report #93, *Ionizing Radiation Exposure of the Population of the United Sates* (1987).

6. National Council on Radiation Protection and Measurements Report #94, *Exposure of the Population in the United States and Canada from Natural Background Radiation* (1987).

7. National Council on Radiation Protection and Measurements Report #95, *Radiation Exposure of the U.S. Population from Consumer Products and Miscellaneous Sources* (1987).

8. National Council on Radiation Protection and Measurements Report #100, *Exposure of the U.S. Population from Diagnostic Medical Radiation* (1989).

9. E. SAMUEL, *Space Station Radiation Shields 'Disappointing'*, NewScientist.com, 19:00 (2002).

10. J. K. SHULTIS, R. E. FAW, *Radiation Shielding*, Prentice Hall PTR (1996).

11. NCRP Report No. 142, *Operational Radiation Safety Program for Astronauts in Low-Earth Orbit: A Basic Framework*, National Council on Radiation Protection and Measurements (2002).

12. Http://www.tpub.com/doenuclearphys/index.htm, *DOE Nuclear Physics* (2003).

13. J. H. HEINBOCKEL, J. W. WILSON, R. C. SINGLETERRY, M. S. CLOWDSLEY, G. A. FELDMAN, *A Fast Nonperturbative Method for Neutron Transport*, DOE Low Dose Radiation Research Program Workshop II and NASA 12th Annual Space Radiation Health Investigators Workshop, Washington, D.C. (2001).

14. G. I. BELL, S. GLASSTONE, *Nuclear Reactor Theory*, Van Nostrand Reinhold Company, New York (1970).

15. J. W. HAFFNER, *Radiation and Shielding in Space*, Academic Press (1967).

16. J. W. WILSON, F. F. BADAVI, F. A. CUCINOTTA, J. L. SHINN, G. D. BADHWAR, R. SILBERBERG, C. H. TSAO, L. W. TOWNSEND, R. K. TRIPATHI, *HZETRN: Description of a Free-Space Ion and Nucleon Transport and Shielding Computer Program*, NASA TP-3495, National Aeronautics and Space Administration (1995).

17. M. S. CLOWDSLEY, J. W. WILSON, J. H. HEINBOCKEL, R. K. TRIPATHI, R. C. SINGLETERRY, J. L. SHINN, *An Improved Elastic and Non-Elastic Neutron Transport Algorithm for Space Radiation*, NASA TP-99-3335, National Aeronautics and Space Administration (1999).

18. M. S. CLOWDSLEY, J. H. HEINBOCKEL, H. KANEKO, J. W. WILSON, R. C. SINGLETERRY, J. L. SHINN, *A Comparison of the Multigroup and Collocation Methods for Solving the Low-Energy Neutron Boltzmann Equation*, Canadian Journal of Physics, 78:45-56 (2000).

19. L. S. WATERS, *MCNPX User's Manual*, Version 2.3.0, LA-UR-02-2607 (2002).

20. R. C. SINGLETERRY JR., J. W. WILSON, M. S. CLOWDSLEY, J. H. HEINBOCKEL, *Enhanced Low Energy Neutron Transport Modeling for the High Charge and Energy Transport Code HZETRN*, Proceedings International Conference on Mathematics and Computation, Reactor Physics and Environment Analysis in Nuclear Applications, Madrid, Spain (1999).

21. Http://t2.lanl.gov/cgi-bin/endind, *Index to ENDF/B-VI Neutron Data* (2003).

22. J. H. HEINBOCKEL, G. A. FELDMAN, J. W. WILSON, R. C. SINGLETERRY, M. S. CLOWDSLEY, *Solutions to the Low Energy Neutron Boltzmann Equation for Space Applications*, Society of Automotive Engineers, Inc. (2001).

23. E. E. LEWIS, W. F. MILLER JR., *Computational Methods of Neutron Transport*, John Wiley & Sons, Inc. (1984).

APPENDIX A

LIST OF UNITS

The forward-backward model solves the coupled system of Boltzmann equations (4.12) and (4.13), namely

$$\mu\frac{\partial\Phi_F(x,E)}{\partial x}+\sigma(E)\Phi_F(x,E)$$

$$=\sum_m\left[\int_E^{E/\alpha_m^*}f_m(E,E')\Phi_F(x,E')dE'+\int_{E/\alpha_m^*}^{E/\alpha_m}f_m(E,E')\Phi_B(x,E')dE'\right]+Q_F(x,E)$$

and

$$\mu\frac{\partial\Phi_B(x,E)}{\partial x}+\sigma(E)\Phi_B(x,E)$$

$$=\sum_m\left[\int_E^{E/\alpha_m^*}f_m(E,E')\Phi_B(x,E')dE'+\int_{E/\alpha_m^*}^{E/\alpha_m}f_m(E,E')\Phi_F(x,E')dE'\right]+Q_B(x,E)$$

The following is a list of variables and corresponding units of measurement that are used in the forward-backward model.

$$[\Phi_B(x,E)]=\frac{\#\text{ of neutrons}}{\text{cm}^2-\text{MeV}}, \tag{A.1}$$

$$[\Phi_F(x,E)]=\frac{\#\text{ of neutrons}}{\text{cm}^2-\text{MeV}}, \tag{A.2}$$

$$[x] = \frac{\mathrm{g}}{\mathrm{cm}^2}, \tag{A.3}$$

$$[E] = \mathrm{MeV}, \tag{A.4}$$

$$[E'] = \mathrm{MeV}, \tag{A.5}$$

$$[\sigma(E)] = \frac{\mathrm{cm}^2}{\mathrm{g}}, \tag{A.6}$$

$$[f_m(E,E')] = \text{ dimensionless}, \tag{A.7}$$

$$[Q_B(x,E)] = \frac{\#\text{of neutrons}}{\mathrm{g}-\mathrm{MeV}}, \tag{A.8}$$

$$[Q_F(x,E)] = \frac{\#\text{of neutrons}}{\mathrm{g}-\mathrm{MeV}}, \tag{A.9}$$

$$\text{and } [\mu] = \text{ dimensionless}. \tag{A.10}$$

The notation [] is read as "the dimension of" in equations (A.1) through (A.10).

APPENDIX B

TRUNCATION ERROR

Following the analysis in reference [23], the truncation error associated with using difference approximations to solve linear first order differential equations is investigated. Consider the linear first order differential equation

$$\frac{d}{dx}\Phi(x)+\lambda\Phi(x)=S(x), \tag{B.1}$$

where λ is a real constant and $S(x)$ is an arbitrary function of x. The solution to equation (B.1) satisfies the boundary condition $\Phi(0)=\Phi_0$. To solve equation (B.1) using uniform difference spacing of the form $x_j = jh$, where h represents the spacing between grid points, first evaluate equation (B.1) at x_j. Doing this evaluation gives

$$\frac{d}{dx}\Phi(x)\Big|_{x_j}+\lambda\Phi(x_j)=S(x_j). \tag{B.2}$$

Using a forward difference approximation to the derivative in equation (B.2), approximate equation (B.1) with the difference equation

$$\frac{\Phi_{j+1}-\Phi_j}{h}+\lambda\Phi_j=S_j. \tag{B.3}$$

In equation (B.3), Φ_j and S_j are short hand notations for $\Phi(x_j)$ and $S(x_j)$, respectively.

Local truncation error τ for the forward difference approximation is defined as

$$\tau=\frac{\Phi_{j+1}-\Phi_j}{h}+\lambda\Phi_j-S_j. \tag{B.4}$$

Difference equation (B.3) is consistent if $\tau\to 0$ as $h\to 0$. If Φ is a smooth function of x,

then expanding Φ_{j+1} in a Taylor series gives

$$\Phi_{j+1} = \Phi_j + h\frac{d\Phi}{dx}\bigg|_{x_j} + \frac{h^2}{2}\frac{d^2\Phi}{dx^2}\bigg|_{x_j} + \frac{h^3}{6}\frac{d^3\Phi}{dx^3}\bigg|_{x_j} + \cdots. \tag{B.5}$$

Substituting equation (B.5) into equation (B.4) gives

$$\tau = \lambda\Phi_j - S_j + \frac{d\Phi}{dx}\bigg|_{x_j} + \frac{h}{2}\frac{d^2\Phi}{dx^2}\bigg|_{x_j} + \frac{h^2}{6}\frac{d^3\Phi}{dx^3}\bigg|_{x_j} + \cdots. \tag{B.6}$$

Equation (B.2) eliminates the first three terms on the right hand side of equation (B.6), giving

$$\tau = \frac{h}{2}\frac{d^2\Phi}{dx^2}\bigg|_{x_j} + \frac{h^2}{6}\frac{d^3\Phi}{dx^3}\bigg|_{x_j} + \cdots. \tag{B.7}$$

As the spacing between grid points becomes smaller, the first term on the right hand side of equation (B.7) becomes the leading order term. All other terms are negligibly small compared to the leading order term, and the local truncation error for forward differencing is of order h.

Use the expression

$$\frac{d\Phi}{dx}\bigg|_{x_j} \approx \frac{\Phi_j - \Phi_{j-1}}{h} \tag{B.8}$$

for the backward difference approximation to the derivative. The difference equation approximation to equation (B.1) is expressed as

$$\frac{\Phi_j - \Phi_{j-1}}{h} + \lambda\Phi_j = S_j. \tag{B.9}$$

Local truncation error τ for the backward difference approximation is defined as

$$\tau = \frac{\Phi_j - \Phi_{j-1}}{h} + \lambda\Phi_{j-1} - S_{j-1}. \tag{B.10}$$

Difference equation (B.9) is consistent if $\tau \to 0$ as $h \to 0$. If Φ is a smooth function of x,

then expanding Φ_j in a Taylor series gives

$$\Phi_j = \Phi_{j-1} + h\frac{d\Phi}{dx}\Big|_{x_{j-1}} + \frac{h^2}{2}\frac{d^2\Phi}{dx^2}\Big|_{x_{j-1}} + \frac{h^3}{6}\frac{d^3\Phi}{dx^3}\Big|_{x_{j-1}} + \cdots. \tag{B.11}$$

Substituting equation (B.11) into equation (B.10) gives

$$\tau = \lambda\Phi_{j-1} - S_{j-1} + \frac{d\Phi}{dx}\Big|_{x_{j-1}} + \frac{h}{2}\frac{d^2\Phi}{dx^2}\Big|_{x_{j-1}} + \frac{h^2}{6}\frac{d^3\Phi}{dx^3}\Big|_{x_{j-1}} + \cdots. \tag{B.12}$$

Evaluate equation (B.2) at grid point x_{j-1}. The resulting expression eliminates the first three terms on the right hand side of equation (B.12), giving

$$\tau = \frac{h}{2}\frac{d^2\Phi}{dx^2}\Big|_{x_{j-1}} + \frac{h^2}{6}\frac{d^3\Phi}{dx^3}\Big|_{x_{j-1}} + \cdots. \tag{B.13}$$

As the spacing between grid points becomes smaller, the first term on the right hand side of equation (B.13) becomes the leading order term. All other terms are negligibly small compared to the leading order term, and the local truncation error for backward differencing is of order h.

APPENDIX C

STABILITY AND CONVERGENCE

Following the analysis in Reference [23], the stability and convergence of numerical solutions to linear first order differential equations when using difference approximations is investigated. Consider the spatial interval $0 \le x \le L$, and divide this interval into J subintervals having grid spacing $h = L/J$. Solve for the J values $\Phi_1, \Phi_2, \Phi_3, ..., \Phi_J$ by taking the finite difference approximations given in Appendix B and applying them to equation (B.1). The finite difference equation solution Φ_j converges to the true solution $\Phi(x_j)$ if $\Phi_j \to \Phi(x_j)$ as $h \to 0$, where $j = 1, 2, 3, \ldots, J$. A finite length interval requires $J \to \infty$ as $h \to 0$.

Since τ is of order h, as shown in Appendix B, as the grid spacing approaches zero so does the truncation error. The difference equations are consistent when they converge to the true solution, and there is zero truncation error as the grid spacing goes to zero. The difference equations are unstable if the truncation error introduced at each grid point grows for successive values of j. In an unstable system of finite difference equations, the rounding off to a finite number of decimal places by a digital computer introduces some error at each grid point. As the total number of steps gets larger in an unstable system, rounding off error grows until the solution is no longer valid. The system is stable if errors diminish in magnitude as the number of steps increases. Finite difference equations converge to the true solution in a stable system.

Using the same notation developed in Appendix B, let $S_j = 0$ in equation (B.2).

The exact solution to the resulting equation is

$$\Phi(x_j) = \Phi_0 \exp(-\lambda x_j), \tag{C.1}$$

where $\Phi_0 = \Phi(0)$ and $x_j = jh$.

From equation (B.3), the forward difference equation takes the form

$$\Phi_{j+1} = (1 - h\lambda)\Phi_j. \tag{C.2}$$

It follows that

$$\Phi_j = (1 - h\lambda)^j \Phi_0. \tag{C.3}$$

Rewrite equation (C.3) as

$$\Phi_j = \Phi_0 \exp[\ln(1 - h\lambda)^j]. \tag{C.4}$$

Equation (C.4) can be written in the form

$$\Phi_j = \Phi_0 \exp[j \ln(1 - h\lambda)]. \tag{C.5}$$

Finally, equation (C.5) is equivalent to

$$\Phi_j = \Phi_0 \exp\left\{-\frac{\ln[1/(1 - h\lambda)]}{h\lambda}\lambda x_j\right\}. \tag{C.6}$$

Equation (C.6) converges to the exact solution only if $\ln[1/(1 - h\lambda)]/(h\lambda) \to 1$ as $h \to 0$.

Expanding $\ln[1/(1 - h\lambda)]/(h\lambda)$ for $1/(1 - h\lambda) > 0$ gives

$$\frac{\ln[1/(1 - h\lambda)]}{h\lambda} = \frac{2}{h\lambda}\left[\frac{1/(1 - h\lambda) - 1}{1/(1 - h\lambda) + 1} + \frac{1}{3}\left(\frac{1/(1 - h\lambda) - 1}{1/(1 - h\lambda) + 1}\right)^3 + \frac{1}{5}\left(\frac{1/(1 - h\lambda) - 1}{1/(1 - h\lambda) + 1}\right)^5 + \cdots\right]. \tag{C.7}$$

Equation (C.7) simplifies to

$$\frac{\ln[1/(1 - h\lambda)]}{h\lambda} = \frac{2}{h\lambda}\left[\frac{h\lambda}{2 - h\lambda} + \frac{1}{3}\left(\frac{h\lambda}{2 - h\lambda}\right)^3 + \frac{1}{5}\left(\frac{h\lambda}{2 - h\lambda}\right)^5 + \cdots\right]. \tag{C.8}$$

Equation (C.8) can be written as

$$\frac{\ln[1/(1-h\lambda)]}{h\lambda} = 2\left[\frac{1}{2-h\lambda} + \frac{(h\lambda)^2}{3}\left(\frac{1}{2-h\lambda}\right)^3 + \frac{(h\lambda)^4}{5}\left(\frac{1}{2-h\lambda}\right)^5 + \cdots\right]. \tag{C.9}$$

Letting $h \to 0$ gives $\ln[1/(1-h\lambda)]/(h\lambda) \to 1$. The numerical solution converges to the exact solution for forward difference approximations.

From equation (B.9), the backward difference equation takes the form

$$\mathbf{\Phi}_j = \frac{1}{1+h\lambda}\mathbf{\Phi}_{j-1}. \tag{C.10}$$

Equation (C.10) can be expressed in the equivalent form

$$\mathbf{\Phi}_{j+1} = \frac{1}{1+h\lambda}\mathbf{\Phi}_j. \tag{C.11}$$

It follows that

$$\mathbf{\Phi}_j = \left(\frac{1}{1+h\lambda}\right)^j \mathbf{\Phi}_0. \tag{C.12}$$

Rewrite equation (C.12) in the form

$$\mathbf{\Phi}_j = \mathbf{\Phi}_0 \exp\left[\ln\left(\frac{1}{1+h\lambda}\right)^j\right]. \tag{C.13}$$

Equation (C.13) can be written as

$$\mathbf{\Phi}_j = \mathbf{\Phi}_0 \exp\left[j\ln\left(\frac{1}{1+h\lambda}\right)\right]. \tag{C.14}$$

Finally, equation (C.14) is equivalent to

$$\mathbf{\Phi}_j = \mathbf{\Phi}_0 \exp\left\{\frac{\ln[1/(1+h\lambda)]}{h\lambda}\lambda x_j\right\}. \tag{C.15}$$

Equation (C.15) converges to the exact solution only if

$\ln[1/(1+h\lambda)]/(h\lambda) \to -1$ as $h \to 0$. Expanding $\ln[1/(1+h\lambda)]/(h\lambda)$ for $1/(1+h\lambda) > 0$ gives

$$\frac{\ln[1/(1+h\lambda)]}{h\lambda} = \frac{2}{h\lambda}\left[\frac{1/(1+h\lambda)-1}{1/(1+h\lambda)+1} + \frac{1}{3}\left(\frac{1/(1+h\lambda)-1}{1/(1+h\lambda)+1}\right)^3 + \frac{1}{5}\left(\frac{1/(1+h\lambda)-1}{1/(1+h\lambda)+1}\right)^5 + \cdots\right]. \quad \text{(C.16)}$$

Equation (C.16) simplifies to

$$\frac{\ln[1/(1+h\lambda)]}{h\lambda} = \frac{2}{h\lambda}\left[\frac{-h\lambda}{2+h\lambda} + \frac{1}{3}\left(\frac{-h\lambda}{2+h\lambda}\right)^3 + \frac{1}{5}\left(\frac{-h\lambda}{2+h\lambda}\right)^5 + \cdots\right]. \quad \text{(C.17)}$$

Equation (C.17) can be written as

$$\frac{\ln[1/(1+h\lambda)]}{h\lambda} = 2\left[\frac{-1}{2+h\lambda} + \frac{(h\lambda)^2}{3}\left(\frac{-1}{2+h\lambda}\right)^3 + \frac{(h\lambda)^4}{5}\left(\frac{-1}{2+h\lambda}\right)^5 + \cdots\right]. \quad \text{(C.18)}$$

Letting $h \to 0$ gives $\ln[1/(1+h\lambda)]/(h\lambda) \to -1$. The numerical solution converges to the exact solution for backward difference approximations.

VITA

Gary Alan Feldman was born on September 14, 1960 in Detroit, Michigan. He received an A.A. in Liberal Arts from Oakland Community College in Farmington Hills, Michigan in June 1980. He graduated from Texas A and I University in Kingsville, Texas with a B.S. in Physics in May 1987. He earned a M.S. in Physics from Southwest Texas State University in San Marcos, Texas in August 1990. He was awarded a Ph.D. in Computational and Applied Mathematics from Old Dominion University in Norfolk, Virginia in August 2003.